Journal of
Polymer Materials

Tech Science Press

http://doi.org/10.32604/jpm.2026.084020

ARTICLE

A Fluorescent-Electrochemical Hydrogel Sensing for H_2O_2 and Tartrazine Analysis Based on methacrylamide composite hydrogel materials (MCHM)

Peiqi Zhang[#], Weifeng Chen[#] and Xiaoliang Hao[*]

School of Chemical Engineering, University of Science and Technology Liaoning, Anshan, China
*Corresponding Author: Xiaoliang Hao. Email: haoxiaoliang1980@163.com
[#]These authors contributed equally to this work

Received: 15 April 2026; Accepted: 17 June 2026; Published: 24 September 2026

ABSTRACT: Health remains a persistent focus of research. Currently, many commonly used synthetic dyes are toxic to some extent. Tartrazine is a common synthetic dye used in the food, pharmaceutical, printing, and dyeing industries. Long-term exposure to this substance or its ingestion may pose significant health risks. In addition, oxidizing agents used in water treatment may threaten environmental and human health if they are not properly controlled. Hydrogen peroxide (H_2O_2) is one of the most widely used oxidants and therefore requires effective monitoring. Against this background, this study contributes to the efficient detection of environmentally harmful substances and the development of functional materials. In this study, hydrogels synthesized from methacrylamide (MAM) serve as a template, and carbon quantum dots (CQDs) synthesized from m-phenylenediamine (MPD) are incorporated into the hydrogels. Owing to their porous structure and large specific surface area, a hydrogel material exhibiting blue-green fluorescence is successfully synthesized and named MAM composite hydrogel materials (MCHM). MCHM serve as a bifunctional platform for fluorescent-electrochemical detection, and they effectively reduce the limitations of single-signal detection and enhance the reliability and accuracy of the detection process. This work provides a promising platform for developing functional sensing materials for environmental monitoring and food safety analysis.

KEYWORDS: Tartrazine; fluorescence; hydrogels; electrochemistry; bifunctional

1 Introduction

Health remains a persistent focus of research. Dye wastewater is an important part of industrial wastewater. A large number of residual synthetic dyes in the wastewater has the characteristics of stable chemical properties and is difficult to degrade. If discharged directly without effective treatment, these dyes will not only inflict severe damage on the aquatic ecosystem, but also pose a latent threat to human health through the bioaccumulation effect within the ecosystem's food chain [1]. As a typical water-soluble azo synthetic dye, tartrazine is widely used in food processing, pharmaceutical coating, textile printing, and dyeing. However, such synthetic dyes not only do not serve the purpose of supplementing the nutritional requirements of human beings, but also may cause irreversible harm to the human body to a certain extent [2]. When the human body consumes tartrazine at high concentrations, the metabolic process of tartrazine can substantially augment the filtration and excretion load on the kidneys, thereby disrupting their normal physiological functions. Relevant studies have shown that tartrazine metabolites may exhibit genotoxicity, and long-term cumulative exposure may increase the risk of cancer and adversely affect

the immune and reproductive systems [3,4]. Common methods for the detection of tartrazine include high-performance liquid chromatography and capillary electrophoresis [5].

Meanwhile, hydrogen peroxide (H_2O_2), as a green and strong oxidant, occupies an important position in the field of life and medical and other industries due to its high efficiency of disinfection, simple decomposition products, and no pollution residue. In daily life, it is often used in scenarios such as wound cleaning and disinfecting the home environment. In the medical field, it can be used as a mucous membrane disinfectant, an instrument sterilization agent to assist clinical diagnosis and treatment [6,7]. In industrial production, it is a key additive for paper bleaching and wastewater treatment. In the food industry, it is used in food preservation, fruit and vegetable cleaning to extend the shelf life of food and reduce the risk of microbiological contamination. However, the dosage and range of H_2O_2 need to be strictly controlled, and if overdosed, it may cause serious damage to the organism [8–10]. Direct contact with high concentrations of H_2O_2 may corrode skin and mucous membrane tissues, causing symptoms such as redness, swelling, pain, and even ulceration. When excessive H_2O_2 enters the human body, it will break the dynamic balance of the redox system in the body [11–13], prompting the generation of a large number of reactive oxygen radicals, which will attack the biological macromolecules (such as proteins, lipids, nucleic acids, etc.) [14–16], thereby damaging cellular structure and function and potentially inducing inflammation and accelerating cellular aging in the long run or after repeated exposure. Commonly used methods for the detection of H_2O_2 include potassium permanganate titration and enzyme-catalyzed methods [17–19].

M-phenylenediamine (MPD) is recognized as a mature, low-cost, and versatile precursor for carbon quantum dots (CQDs) synthesis. Featuring high reactivity, outstanding optical characteristics, and desirable biocompatibility, MPD has been found to have broad applications in fluorescent sensing, bioimaging, and environmental analysis.

Hydrogels are formed by the chemical cross-linking of hydrophilic polymer chains to create a three-dimensional network structure. They are highly absorbent and do not dissolve after absorbing water [20,21]. Based on the chemical properties of their solutes, hydrogels can be divided into three main categories, which are small molecule solute-based hydrogels, polymer solute-based hydrogels, and nanomaterial composite hydrogels [22]. This paper combines hydrogels with CQDs to synthesize a novel composite hydrogel materials (MCHM), which falls within the category of nanocomposite hydrogels. The materials exhibit good biocompatibility, and their microstructure can be controlled by adjusting the reaction conditions. Moreover, recognition sites can be introduced through functional modification, making them suitable for research into fluorescent detection and electrochemical sensing [23,24]. MCHM possess a porous structure and a high specific surface area, offering excellent stability whilst also ensuring superior loading capacity. By incorporating CQDs through appropriate synthesis techniques and regulating their release rate via a controlled-release system, the service life can be extended, thereby achieving the ideal release profile for this experiment. The materials offer significant structural advantages and hold great promise for applications in the field of detection [25–28]. Compared with single-network hydrogels, a double-network structure can further enhance the performance of fluorescent-electrochemical sensing [29,30].

In addition, a three-dimensional network structure possesses excellent elastic responsiveness, and its porous structure can dynamically adjust itself according to the size of target analytes, enabling automatic adaptability to both macromolecules and small molecules to facilitate their diffusion and interaction with the hydrogel matrices. When analyzing small molecules, hydrogels exhibit a molecular sieving effect due to their pore size, which prevents large molecular impurities from entering and affecting the results. According to relevant literature, researchers have prepared sodium alginate hydrogels for the detection of uric acid,

which successfully blocked macromolecules such as globulins [31,32]. This paper selects tartrazine and H_2O_2 as the target analytes, accurately reflecting the test results.

A large number of studies indicate that hydrogels have been widely adopted in the field of analytical testing for various substances. MCHM constructed in this study can achieve high-sensitivity and high-accuracy detection of tartrazine and H_2O_2 in industrial wastewater. MCHM offer significant practical value and are expected to be widely adopted in environmental monitoring and everyday testing applications [33–36].

Meanwhile, MCHM have good functional designability, which can be used to achieve rapid response and detection of target substances, such as tartrazine and H_2O_2, by introducing fluorescent groups, conductive components, or specific recognition units into the network [25,27,28]. The hydrophilicity allows MCHM to disperse rapidly and remain stable in water, thereby facilitating accurate testing and providing an efficient, sensitive, and stable platform for water quality and food testing [37]. At present, functional materials have become the core driving force to promote technological innovation in many fields, and are widely used in new energy material preparation, drug target delivery, environmental pollutant monitoring, treatment, and other key areas [38–42]. According to relevant literature, MCHM have been successfully used in clinical wound microenvironment monitoring due to their excellent biocompatibility and rapid response [43–47]. By utilizing the oxidation of H_2O_2 in wound exudate to activate hydrogel monomers [48–50], they can accurately detect the concentration of H_2O_2 during infection, offering a novel strategy for chronic wound diagnosis and treatment [51–55]. Research on composite hydrogels for the simultaneous bifunctional detection of tartrazine and H_2O_2 are still limited, and related detection materials still suffer from problems such as a single detection mode, weak anti-interference ability, and insufficient stability. Based on the aforementioned researches, CQDs are incorporated into the substrate hydrogels to construct MCHM. MCHM can achieve highly sensitive and selective bifunctional detection of tartrazine and H_2O_2 in water via fluorescent-electrochemical signals. This provides a new method for the simultaneous monitoring of complex water environments. Scheme 1 depicts the detection and analysis process of synthetic materials [56–58]. Route (1) depicts the process of preparing CQDs from MPD. Route (2) depicts the process of preparing hydrogels from materials such as MAM, sodium alginate (SA), and polyvinyl alcohol (PVA). Route (3) depicts the electrochemical detection of the reaction changes between the glassy carbon electrode (GCE) and MCHM, which clearly demonstrates the stability of the MCHM, providing a guarantee for subsequent detection. Route (4) depicts the changes in the MCHM before and after detecting tartrazine. Route (5) and Route (6) are used to detect tartrazine and H_2O_2, respectively.

This paper describes the development of a novel fluorescent-electrochemical bifunctional sensor based on MCHM, which enables highly sensitive detection of tartrazine and H_2O_2. Most existing CQDs-based sensors are fabricated using methods such as film coating and powder modification, which often suffer from material detachment, poor stability, and poor reproducibility [59,60]. To overcome these limitations, this study introduces innovations in both material design and methodology. The main innovations of this work are as follows:

(1) MCHM are constructed by using MAM as the substrate and incorporating CQDs into the three-dimensional cross-linked network of the hydrogels. This design not only provides a uniform and anti-aggregation support for CQDs, but also forms continuous electron- and mass-transfer channels. As a result, it resolves the common problems of modifier-layer detachment and signal instability in conventional sensors at the substrate-material level, thereby significantly improving the stability and reproducibility of the overall sensing system.

(2) The synergistic effect of MCHM significantly improves the sensing performance toward both tartrazine and H_2O_2. Conventional CQDs-based sensing systems mainly rely on optical responses and typically show limited electrochemical response capability [61]. The porous structure and conductivity of MCHM further enhance the fluorescent response and electrochemical activity of CQDs. Furthermore, by optimizing the material composition and detection conditions, the proposed sensor achieves a wider linear detection range and lower detection limits for both analytes.

(3) The integrated gel structure of MCHM enables bifunctional fluorescent-electrochemical sensing. The two sensing platforms mutually validate each other, thereby effectively improving detection accuracy. By combining the high conductivity of the hydrogels with the optical properties of CQDs, this material design integrates the advantages of both components and provides a new platform for the detection of tartrazine and H_2O_2.

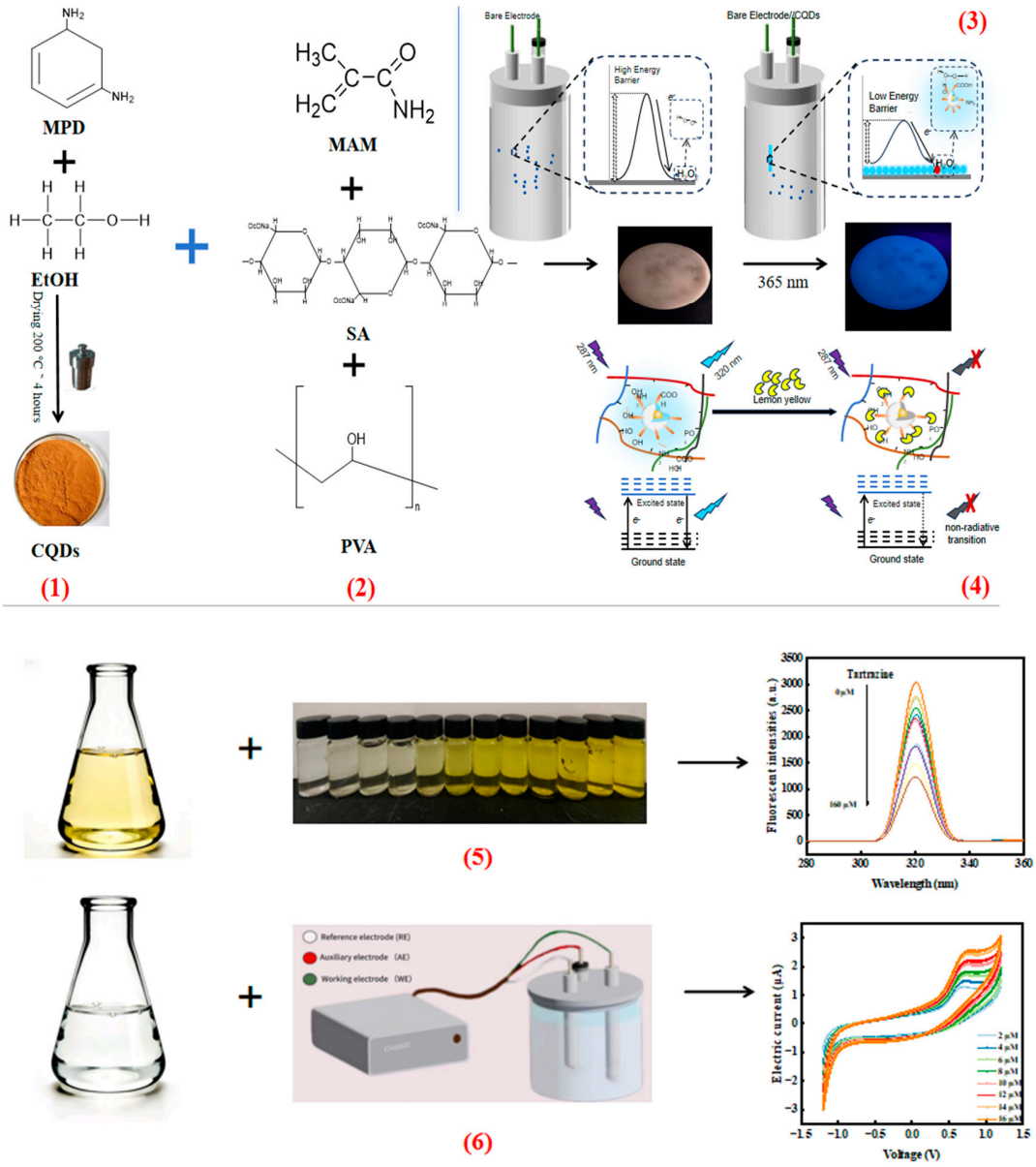

Scheme 1: The detection and analysis process of synthetic materials.

2 Materials and Methods

2.1 Materials

Experimental materials MAM, SA, PVA, anhydrous calcium chloride ($CaCl_2$) and MPD are purchased from Guangdong Yuanfeng Chemical Science and Technology Co., Ltd. H_2O_2, potassium dihydrogen phosphate, dipotassium hydrogen phosphate, and potassium hexacyanoferrate (II) ($[Fe(CN)_6]^{3-/4-}$) are purchased from Shanghai Aladdin Biochemical Technology Co., Ltd. Carrageenan is purchased from Hainan Changqing Agar Factory. Potassium persulphate (KPS) and N, N'-methylenebisacrylamide (Bis) are purchased from Tianjin Huasheng Chemical Reagent Co., Ltd. Deionized water is from the biology laboratory of University of Science and Technology Liaoning. Dialysis membrane (molecular weight cut off 1000 Daltons, Spectra/Por® 7), is purchased from Repligen Co., Ltd.

2.2 Instruments

JEM-2100 transmission electron microscope (TEM), JEOL Ltd.; Zeiss SIGMA HD Field Emission Scanning Electron Microscope (SEM), Carlsbad Management Co., Ltd; Perkin Elmer Spectrum 3 Fourier Transform Infrared Spectroscopy (FTIR), Perkin Elmer Instruments Co., Ltd.; N3 PhiniX X-ray Diffractometer (XRD), Edo Nano Technology (Shanghai) Co., Ltd. MKW-5250 X-ray Photoelectron Spectroscopy (XPS), Shanghai Makeway Semiconductor Technology Co., Ltd. R-210 Rotary Evaporator, BUCHI Labortechnik AG, Switzerland Co., Ltd. DHG-9070A Oven, Shanghai Jinghong Laboratory Instrument Co., Ltd. BUCHI (Switzerland) Co., Ltd. LGJ-10 Freeze dryer, Beijing Songyuan Huaxing Technology Develop Co., Ltd. F-2700 fluorescent Spectrophotometer and U-3900 Ultraviolet-Visible spectroscopy (UV-Vis) spectrophotometer, Hitachi High-Technologies Co., Ltd. CHI660E Electrochemical Workstation, Shanghai Chenhua Instrument Co., Ltd.

This experiment employs a standard three-electrode system: a modified GCE is used as the working electrode, a silver/silver chloride electrode as the reference electrode, and a platinum plate (or platinum wire) as the counter electrode. The GCE has a 3 mm core, an outer rod diameter of 6 mm, a length of 80 mm, and a polytetrafluoroethylene (PTFE) sheath. The silver/silver chloride electrode has a glass tube diameter of 3.8 mm and a length of 50 mm, as well as a PTFE tube diameter of 6 mm and a length of 30 mm. The platinum wire electrode has a purity of 99.99%, with the diameter is 1.0 mm and the height is 37 mm. For platinum wire electrode, the diameter is 1.0 mm and the height is 10 mm. The outer rod diameter is 6 mm, and the total length is 80 mm. The terminals of all three electrodes are 15 mm long. A standard 100 mL three-electrode electrolytic cell is used.

2.3 Preparation of CQDs

Hydrothermal synthesis of the CQDs is carried out as follows: 0.2 g of MPD is weighed and dissolved in 20 mL of deionized water, and the mixture is stirred at room temperature (25°C) for 30 min to obtain a homogeneous solution. The resulting solution is transferred into a 50 mL polytetrafluoroethylene autoclave, ultrasonicated for 10 min, and then subjected to a hydrothermal reaction at 200°C for 4 h [62,63]. After the reaction, the resulting solution is filtered through a 0.22 μm microporous membrane and concentrated under reduced pressure using an R-210 rotary evaporator at 40–45°C. The concentrate is then freeze-dried, ground into a fine powder, and hermetically sealed in sample tubes for storage. The synthesis process is shown in Scheme 1.

2.4 Preparation of Hydrogels Substrate Material

5 g of PVA is dissolved with 40 mL of deionized water at 90°C, heat 30 mL of deionized water to 80–85°C, add 2 g of SA, 1 g of carrageenan and 2 g of gelatin sequentially until all are dissolved. Then mix the solutions completely, and add 0.5 g glycerol; the preparation of the hydrogels substrate material is completed. The synthesis process is shown in Scheme 1.

MAM, PVA, and SA synergistically build the three-dimensional hydrogels network. Polymerized MAM acts as the main skeleton. PVA forms hydrogen bonds to enhance toughness and resilience, while SA forms ionic crosslinks with metal ions, providing greater strength and stimulus responsiveness. These multiple crosslinking modes produce stable and tough hydrogels suitable for the preparation of MCHM.

2.5 Preparation of MCHM

The substrate material is cooled to room temperature, and the fluorescent CQDs solution is added. Then add 5 mL 5% of MAM solution, 0.1 g of Bis, and 0.1 g of KPS. Pour the thoroughly mixed solution into the mould, and then cross-linking is carried out in an oven at 40–45°C for 2 h. Take out the material and put it into the refrigerator and store at −12°C for 12 h and thaw for 2–6 h (cycle this step 3 times) [64]. MCHM are placed in 3% $CaCl_2$ solution for 4 h. After washing with deionized water, the desired MCHM are obtained. The synthesis process is shown in Scheme 1.

In order to combine covalent crosslinking, hydrogen bonding and ionic coordination yield a stable three-dimensional hydrogel network for MCHM fabrication [65]. KPS/Bis-crosslinked MAM builds the covalent skeleton. $CaCl_2$ strengthens mechanics and anti-swelling via ionic coordination. CQDs introduce fluorescence and stabilize the network. The resultant MCHM possess favorable stability, toughness, adjustability and sensing performance.

The obtained MCHM are frozen at −12°C for 24 h, followed by 24 h freeze-drying [66,67]. After fully drying, the samples are ground into fine powder, the powder is sealed in sample tubes for subsequent characterization and testing.

2.6 Fluorescent Analysis of Tartrazine Using MCHM

The viscosity of MCHM is closely related to temperature and the synthesis process. As MCHM are synthesized under fixed conditions, with a consistent volume of liquid added each time, a stable humidity level (80%) is maintained, ensuring that the viscosity of MCHM remains consistent. To ensure the accuracy of the test results, both analysis and testing are carried out at room temperature. The experiment is conducted using a neutral solution.

For fluorescent detection, a dilute MCHM aqueous solution prepared with deionized water is required. After being filtered by dialysis membrane (molecular weight cut off 1000 daltons), analysis and detection are performed under this condition.

Configure the MCHM solution to a concentration of 100 mg/L, dissolve by heating at 40°C, and the tartrazine solutions with concentrations of 0.8 μM, 1.2 μM, 1.6 μM, 4 μM, 8 μM, 12 μM, 16 μM, 40 μM, 80 μM, 120 μM, and 160 μM are configured, respectively [68–70].

2.7 Electrochemical Detection of H_2O_2 by MCHM

The MCHM powder is prepared into a 1 g/L solution, and 8 μL of MCHM is immobilized on the surface of the GCE. Their electrochemical properties are characterized using a CHI660E electrochemical workstation.

Configure 1 mM Phosphate buffered saline (PBS) (pH = 7.5) solution and 5 mM $[Fe(CN)_6]^{3-/4-}$ solution. The electrochemical analysis methods used here include cyclic voltammetry (CV) and electrochemical

impedance spectroscopy (EIS). CV can quickly indicate the redox behavior of MCHM [71–73], and EIS enables a detailed analysis of the impedance [74,75]. The complementarity of the two methods can provide a comprehensive analysis of the electrochemical performance of MCHM.

2.8 Recovery Rate Experiment

In this study, the recovery rates of tartrazine are tested on Xizhilang jelly (orange flavor) and Fanta (orange flavor), which are purchased from supermarkets. The recovery rates of H_2O_2 are evaluated using water samples collected from Xinshi Farm and the Tiexi Water Supply Company in Anshan, Liaoning Province.

3 Results and Discussion

3.1 TEM of CQDs

As can be seen from Fig. 1a, the prepared CQDs exhibit a regular spherical morphology, are well dispersed, and show no obvious agglomeration. The particles are uniform in size, ranging in the nanometre scale, indicating that this method has successfully synthesized CQDs with an ideal morphology and size. Fig. 1b shows that the average diameter size of the CQDs is 4.43 ± 0.03 nm, with a narrow size distribution and good uniformity [76].

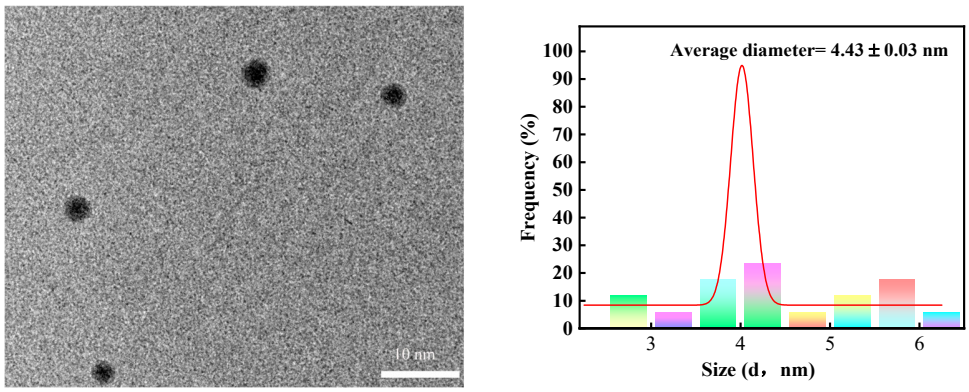

(**a**) (**b**)

Figure 1: (**a**) TEM image of the as-prepared CQDs; (**b**) Particle size distribution histogram, with an average diameter of 4.43 ± 0.03 nm.

3.2 SEM of MCHM

Fig. 2 shows the SEM images of the MCHM powder. Fig. 2a is scanned at 50 X, and the overall morphology of the material is observed. The MCHM powder consists of particle agglomerates that are irregularly stacked to form a large number of micron-sized gaps. Fig. 2b shows the image scanned at 700 X. Further details of the particle surfaces are observed, and the particles exhibit a porous three-dimensional network structure with interconnected pores ranging from a few micrometers to several thousand micrometers. This porous structure enhances the swelling rate of the MCHM, making it suitable for use as a fluorescent gel [77–79]. Fig. 2c shows the image scanned at 3000×. It can be clearly seen that the CQDs are attached to the three-dimensional network system of the MCHM, which are wrapped by the layer by layer, and the MCHM show the 'curled' morphology at the edge of the structure, which is in line with the unique characteristics of the flexible chain of the MCHM. Fig. 2d shows the size distribution of the MCHM [80,81]. The average diameter is 186.76627 ± 1.3493 nm.

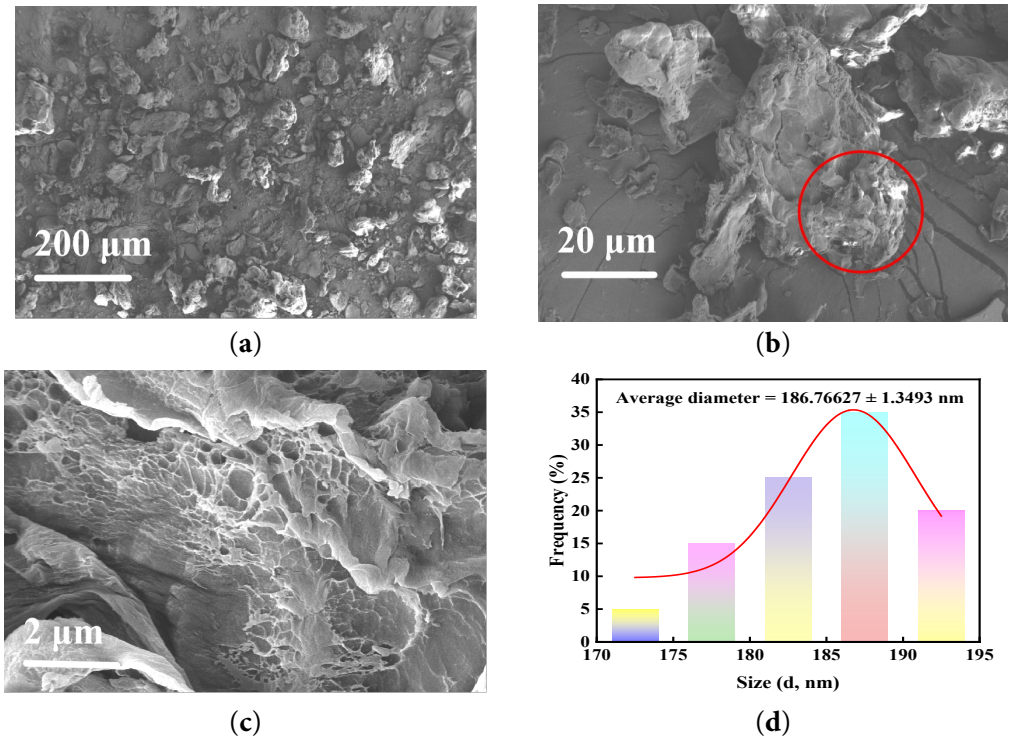

Figure 2: (**a**) 50× SEM image; (**b**) 700× SEM image; (**c**) 3000× SEM image; (**d**) Particle size distribution histogram, with an average diameter of 186.76627 ± 1.3493 nm.

3.3 FTIR and XRD of MCHM

MCHM are a class of extremely hydrophilic three-dimensional network structure gels. They can rapidly absorb water and swell without dissolving in water. When swelling occurs, solvent molecules try to enter into the network structure, causing the volume to swell, leading to the stretching of the three-dimensional molecular network; and the cross-linked molecular chains possess a certain elastic contraction force, causing the hydrogels network to shrink. Fig. 3a shows the results of conducted on MCHM, PVA, SA, MAM, and CQDs. The results show that the prepared fluorescent MCHM successfully incorporate the characteristic functional groups of each precursor. The broadened strong absorption peak near 3300 cm^{-1} is attributed to the inter- and intramolecular hydrogen bonding formed by the large number of -OH contained in the PVA and SA in the system [82,83], which is the key evidence for the formation of the three-dimensional network structure of the hydrogels. The characteristic absorption peaks at 1650 cm^{-1} and 1550 cm^{-1} in the spectra correspond to the amide I band (C=O stretching vibration) and amide II band (N-H bending vibration) in MAM, respectively. In addition, the asymmetric and symmetric stretching vibration peaks of the carboxylate of SA are located near 1650 cm^{-1} (overlapping with the amide I band) and 1400 cm^{-1}, respectively. The broad peaks located in the region of 1000–1250 cm^{-1} are attributed to the stretching vibrations of the glycocyclic ether bond (C-O-C) and the alcohol hydroxyl group (C-OH) [84–86]. The superposition and broadening of the characteristic peaks confirm the formation of a homogeneous composite material through strong hydrogen bonding interactions between the components.

To characterize the structure of MCHM, XRD pattern is analyzed. As can be seen in Fig. 3b, the broadened diffuse peaks presents at $2\theta = 15^{\circ}–30^{\circ}$ reflect the amorphous structural properties of the material. Such broad peaks correspond to the short-range ordered aggregation of atoms, which is one of the typical features of amorphous materials, and it can be clearly demonstrated that the added CQDs play a key role in

MCHM [87,88]. Such structures tend to endow materials with richer surface active sites, higher structural flexibility, and pore tunability, which have potential performance advantages in adsorption, catalysis, energy storage, and other scenarios. The excellent properties of MCHM provide a stable structural foundation for research.

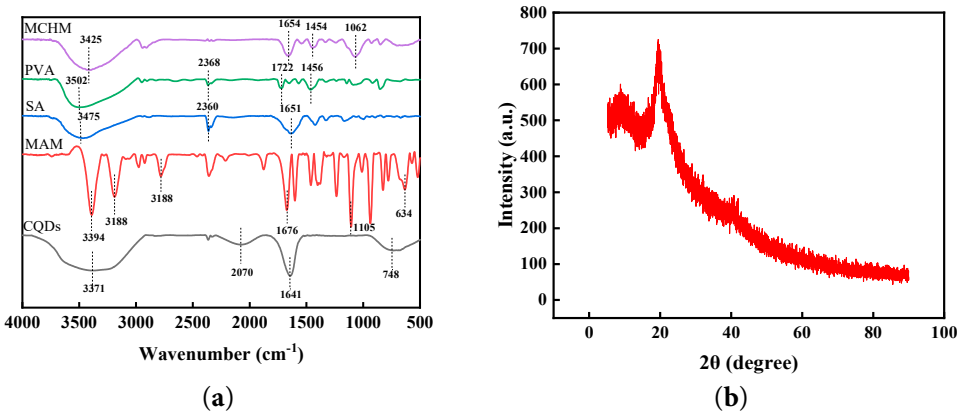

Figure 3: (**a**) FTIR spectra of MCHM, PVA, SA, MAM, and CQDs; (**b**) XRD pattern of synthesized MCHM.

3.4 XPS Results of MCHM

The XPS wide-scan spectrum of MCHM is shown in Fig. 4. Through XPS analysis, it is found that the peak shapes of carbon, nitrogen, oxygen and sulfur elements are relatively regular [89,90]. By judging the peak shapes, the related functional group configurations can be analyzed.

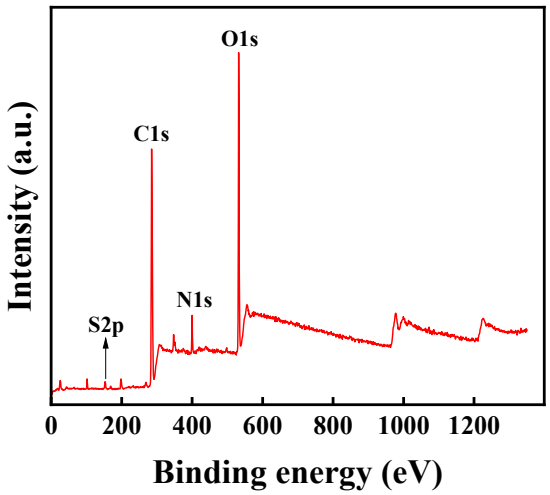

Figure 4: XPS wide-scan survey spectrum of the MCHM. The spectrum clearly shows characteristic peaks corresponding to the elements C (C1s), N (N1s), O (O1s) and S (S2p), confirming the successful incorporation of these elements into the MCHM.

The XPS results show four major peaks at 295, 404, 532 and 192 eV, which are attributed to C1s, N1s, O1s and S2p, respectively (Fig. 4). The high-resolution spectrum displays C=C (284 eV), C-O (285.3 eV), and C=O (286.5 eV) groups (Fig. 5a). This result confirms the coexistence of the carbon intrinsic backbone and oxygen-containing functional groups (e.g., hydroxyl and carbonyl groups) in the material [91]. Fig. 5b shows the presence of the C-N-C group (398 eV) as well, confirming the existence of the C-N bonded structure

and reflecting the involvement of nitrogen in the material in the form of hybridization in the backbone construction. Fig. 5c shows the presence of C-O (531.6 eV) and C=O (532.4 eV) groups in the MCHM structure, further corroborating the variety of oxygen-containing functional groups, complementing the analysis of C1s. The presence of two C-S bonds at 146.6 eV and 169 eV, corresponding to S2p1 and S2p2, i.e., the spin-orbit splitting peaks of S2p in Fig. 5d is able to indicate the presence of elemental S in the MCHM. The results of FTIR, XRD, and XPS reveal the composition of the functional groups of the MCHM [92,93].

The C-S, C-C, C-O, C=O and C-N-C functional groups on the surface of MCHM not only provide stable surface fluorescent states for CQDs, but also offer hydrogen-bonding, electrostatic, and redox active sites for the detection of tartrazine and H_2O_2.

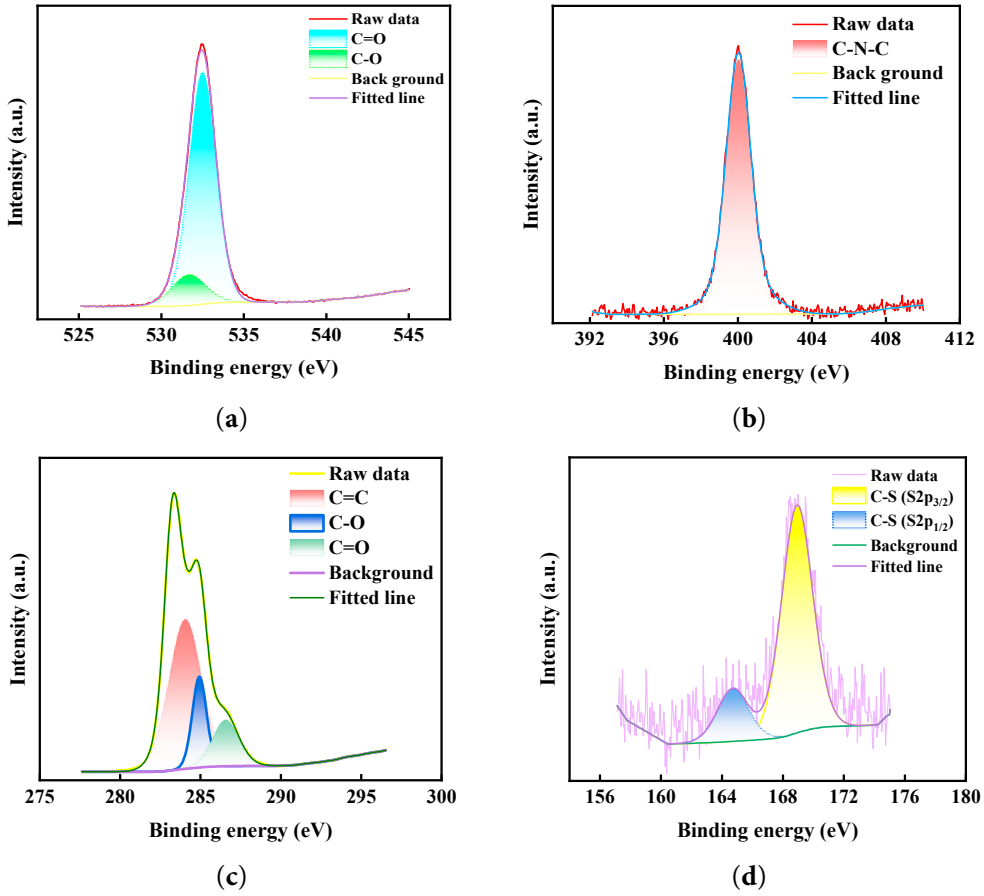

Figure 5: High-resolution XPS spectra and deconvoluted peaks of the MCHM. (**a**) C1s spectrum at ~285 eV, resolved into C=C, C-O, and C=O bonds; (**b**) N1s spectrum at ~400 eV, corresponding to C-N-C bond; (**c**) O1s spectrum at ~532 eV, showing C=O and C-O bonds; (**d**) S2p spectrum at ~169 eV, showing C-S bond. Raw data, background, and fitted curves are presented, confirming the chemical bonding states of S, C, N, and O in MCHM.

3.5 Fluorescent Analysis

3.5.1 Fluorescent Spectral Analysis Results of MCHM

Fig. 6a shows the effect of excitation wavelength in the range of 320–440 nm on the emission. Fig. 6b demonstrates the normalized data of the emission wavelength at different excitation wavelengths, showing that the emission wavelength exhibits a uniform redshift phenomenon, which suggests that the fluorescent properties of the MCHM are significantly correlated with the excitation wavelength. In Fig. 6c, the blue

and red curves correspond to the excitation spectrum (296 nm) and the emission spectrum (320 nm), respectively [94,95]. The UV-Vis absorption spectrum of MCHM (green curve) displays typical selective absorption, with a strong peak at 220–240 nm assigned to the $\pi \rightarrow \pi^*$ transition from the conjugated π-bond system [96,97]. The absorbance decreases sharply to zero above 250 nm, revealing a large energy gap for the electronic transition of conjugated π bonds and providing a foundation for the optical study of MCHM. The international coordinate (x = 0.1552, y = 0.1553) indicates that CQDs emit blue-green fluorescence (Fig. 6d) [98].

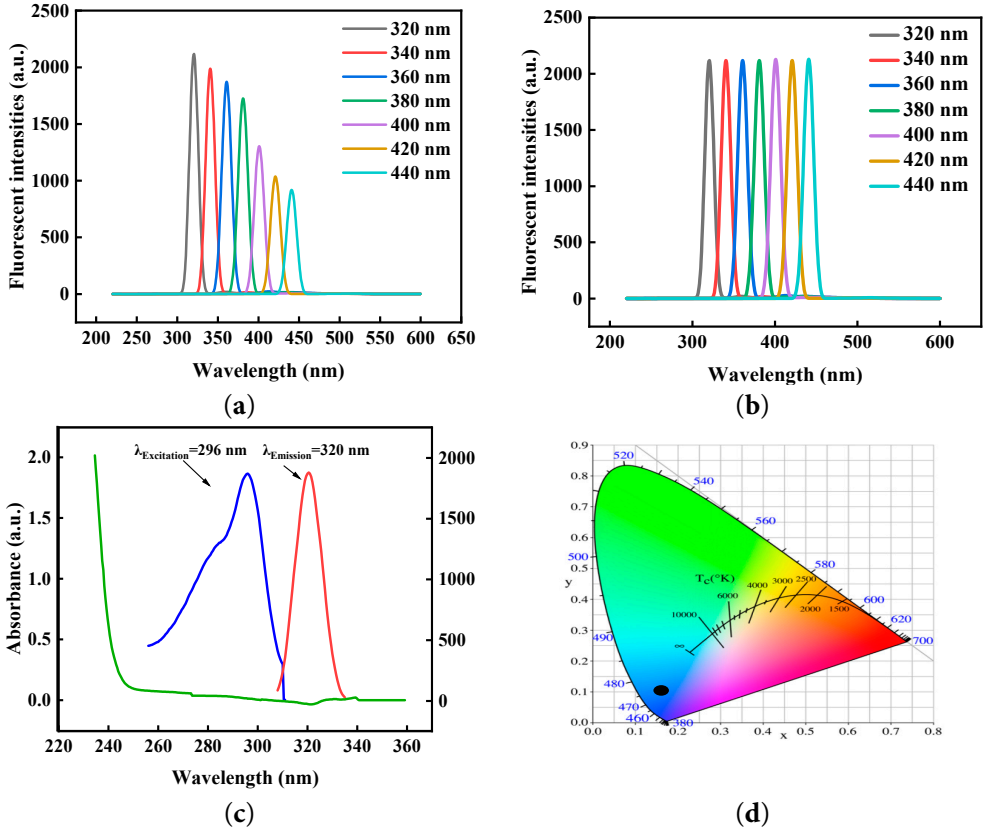

Figure 6: Fluorescent characterization of the MCHM. (**a**) Fluorescent emission spectra recorded under excitation wavelengths ranging from 320 to 440 nm; (**b**) corresponding normalized emission spectra; (**c**) emission spectrum (red line, $\lambda_{emission}$ = 320 nm), excitation spectrum (blue line, $\lambda_{excitation}$ = 296 nm), and UV-vis absorption spectrum (green line); (**d**) International coordinate.

3.5.2 Analysis of Tartrazine by MCHM Based on Fluorescent Mode

The effects of different concentrations (0 to 160 μM) of tartrazine on CQDs are shown in Fig. 7. It can be seen that the fluorescence of CQDs is gradually quenched with the increase of concentration of tartrazine. From Fig. 7a, the linear range (LR) is 0–160 μM, and the detection limit (LOD) is 0.165 μM. Fig. 7b shows the LR of tartrazine. The green curve presents the linear response over the tartrazine concentration range of 0–4 μM, while the blue region shows the linear response in the concentration range of 4–160 μM [99]. The fluorescent intensities of a low-concentration tartrazine solution varies linearly with concentration, as the diluted tartrazine solution exhibits colligative properties, and intermolecular forces are weak. As the concentration increases, the intermolecular distance decreases, and interactions intensify, leading to fluorescent quenching. Fig. 7c illustrates the changes in fluorescent intensities over four cycles. During

each cycle, the fluorescent intensities fluctuate between high and low values with minimal error, indicating that the material exhibits good reproducibility. Fig. 7d illustrates the quenching time of tartrazine. With the increase of time, it shows a rapid decay from 0–10 min, and then gradually tends to be stable after 10 min.

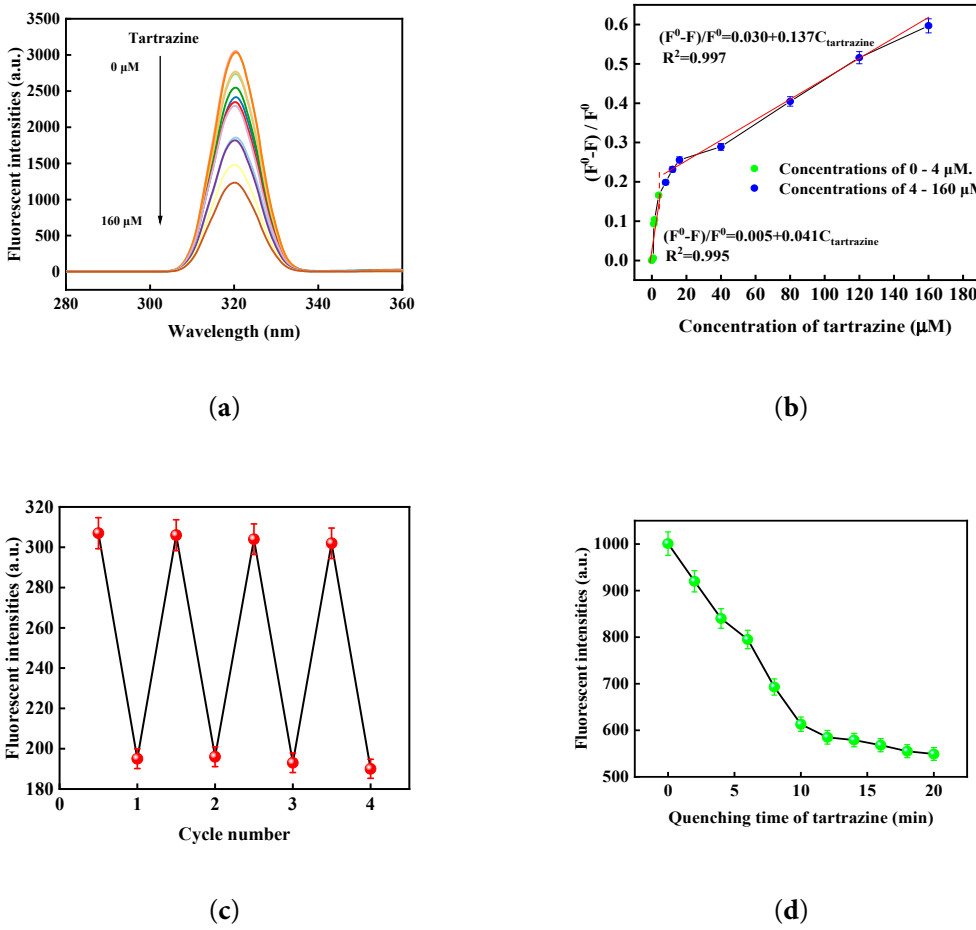

Figure 7: (**a**) Quenching spectra; (**b**) Quenching curve, green points present a linear curve (0–4 μM); blue points present a linear curve (4–160 μM); (**c**) Reciprocal property of fluorescent reproducibility; (**d**) Quenching time of tartrazine. F^0 presents the initial fluorescent intensity; F presents the fluorescent intensity after adding tartrazine, (F^0-F/F^0) presents quenching rates, R^2 presents the coefficient of determination.

3.5.3 Experimental Results of Tartrazine Recovery Rates

In Table 1, it can be clearly seen that the recovery rate of XizhiLang jelly can reach 98.587%, and the relative standard deviation (RSD) is as low as 2.549%; The recovery rate of Fenda soft drink can reach 97.183%, and the RSD is as low as 2.083%. The recovery rates of both sets of RSDs are between 95% and 100%, indicating that the detection method has good accuracy. Two sets of RSDs are less than 3%, and the results of multiple parallel measurements are stable, meeting the requirements for analysis and detection [66].

3.5.4 Mechanism Analysis of Tartrazine

Two-dimensional correlation spectroscopy (2D-COS) is used to analyze and validate the fluorescent property analysis. Fig. 8a shows the fluorescent synchrony of MCHM. The horizontal axis is the emission wavelength, the vertical axis is the excitation wavelength, and the color corresponds to the fluorescent

intensities. In order to reveal the changes of the fluorescent components in CQDs under different conditions, the excitation effect of the substance on tartrazine in the concentration range of 0–160 μM is investigated. A high fluorescent region (blue-green dots) appeared at (excitation ≈ 296 nm, emission ≈ 320 nm), indicating that the fluorescent signals of CQDs under this condition are concentrated and of high intensities, with peaks up to 3.7×10^4 [100–102].

Table 1: Fluorescent recovery rates.

Sample	Spiked Concentration (μM)	Total Found (μM)	Recovery Rates (%)	RSDs (%)
Xizhilang jelly (orange flavor)	1	0.989	98.90	3.607
	2	1.957	97.90	2.114
	4	3.960	99.00	1.926
Fanta (orange flavor)	1	0.973	97.30	2.223
	2	1.927	96.36	1.845
	4	3.916	97.90	2.173

Fig. 8b shows the fluorescent asynchronous mapping of CQDs. The results indicate the dynamic change process of different fluorescent components in MCHM and their interactions. In this figure, a significant automatic peak located at excitation/emission ≈ 370/518 nm is observed on the diagonal, indicating a homogeneous positive correlation change of the corresponding component under perturbation. Characteristic cross peaks appear on both sides of the diagonal, with a pair of cross peaks of opposite sign at (296 nm, 592 nm) and (592 nm, 296 nm) coordinates, indicating that the sample is not a single component, but a complex system containing multiple components with independent response behaviours, and that the changes of different components are not synchronized as they follow their own unique kinetic paths under the external perturbation.

In Fig. 8a, a single and symmetric automatic peak can be observed near 300 nm, with no other cross peaks present. This indicates that there is only one fluorescent component in the system. The addition of tartrazine does not result in the appearance of any new fluorescent components, suggesting that the quenching is static. In Fig. 8b, it can be observed that the fluorescent intensities exhibit a decreasing trend as the concentration of tartrazine increases. According to an analysis of 2D-COS, the interaction between tartrazine and MCHM, through intermolecular forces such as hydrogen bonding and van der Waals forces, leads to a significant decrease in quenching intensity as the concentration of tartrazine increases [103,104].

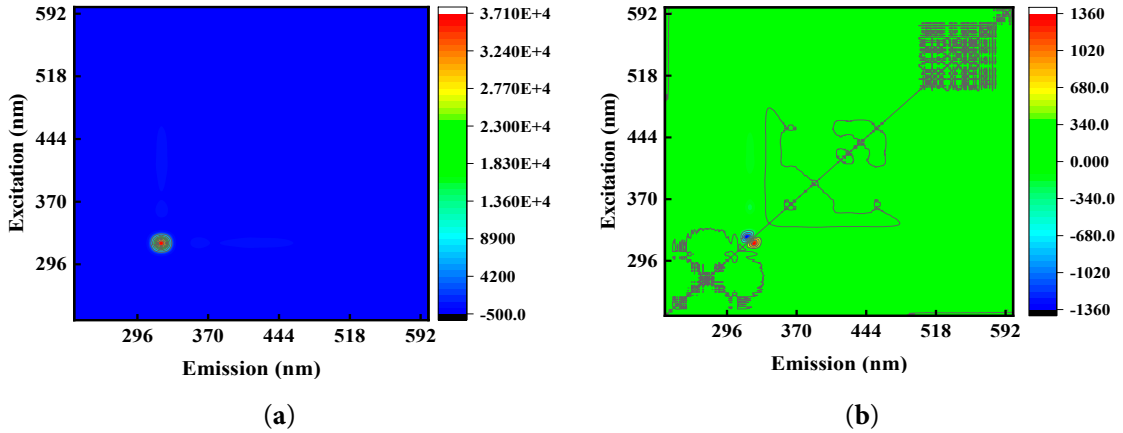

Figure 8: (**a**) Fluorescent synchronous spectroscopy; (**b**) Fluorescent asynchronous spectroscopy.

3.6 Using MCHM to Detect H_2O_2 Based on the Electrochemical Platform

3.6.1 Conditional Optimization

As shown in Fig. 9, the MCHM system exhibits the highest current response and the largest integrated area of the CV curves among all samples, indicating that MCHM possess superior charge-transfer capability and electrochemical activity. In contrast, the CV method response of the hydrogels system decreases to varying degrees when any key component is removed, demonstrating that each structural unit plays an important role in improving the overall electrochemical performance of the material.

Specifically, the hydrogel without CQDs shows a significantly reduced current response, indicating that CQDs provide electrochemically active sites and facilitate electron transfer. In the absence of MAM, the primary network skeleton cannot be fully constructed, resulting in decreased continuity of conductive pathways and reduced interfacial stability, thereby weakening the overall electrochemical response. When SA/Ca^{2+} is absent, the ionic crosslinked network is disrupted, leading to reduced structural compactness and weakened synergistic mass-transfer capability within the material. The sample without freeze-thaw treatment also exhibits inferior structural stability and transport efficiency compared with the MCHM due to the insufficient formation of the PVA physically crosslinked network.

Overall, the excellent electrochemical performance of MCHM arises from the synergistic effects among the MAM chemically polymerized frameworks, the PVA freeze-thaw-induced physically crosslinked networks, the SA/Ca^{2+} ionically crosslinked structures, and the electrochemically active centers of CQDs. The three-dimensional network constructed by multiple crosslinking mechanisms not only enhances the structural stability and integrity of the material, but also provides more efficient pathways for electron transfer and mass diffusion, thereby enabling MCHM to exhibit the best performance in electrochemical detection.

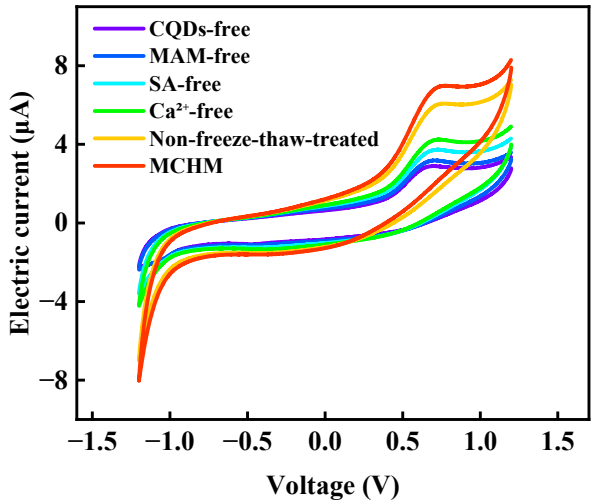

Figure 9: CV curves of hydrogels with different formulations, including CQDs-free, MAM-free, SA-free, Ca^{2+}-free, non-freeze-thaw-treated hydrogels, and MCHM.

Fig. 10a shows the volume optimization experiment is 2–10 μL of MCHM solution is applied to the surface of each of the five working electrodes. The results indicate that the coulombic efficiency varies during testing. Conductivity increases with increasing MCHM volume; however, when the MCHM volume is too high, electron transfer is hindered. Fig. 10b shows the voltage optimization experiment, with the measurement range set between −0.5 V and −0.7 V; as the voltage changes, the coulombic efficiency also changes accordingly. Excessively high voltages can cause other substances within the material to undergo

reduction reactions, thereby affecting the electrical conductivity of the MCHM. Fig. 10c shows the pH optimization experiment is the pH of the electrolyte (PBS solution) ranging from 6.0 to 8.0; an excessively high pH leads to a decrease in the coulombic efficiency, thereby affecting the experimental results. The test conditions are determined is volume of 8 μL, voltage of −0.6 V, pH = 7.5 as the optimal conditions [105].

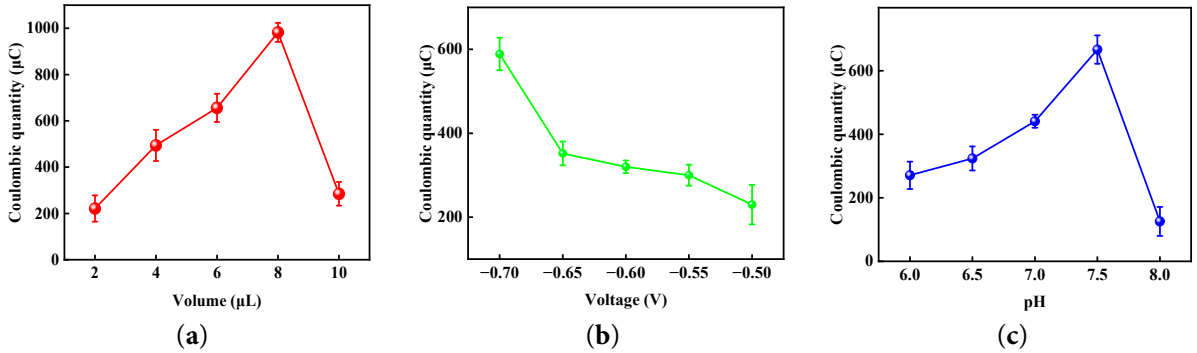

Figure 10: (**a**) Volume optimization; (**b**) Voltage optimization; (**c**) pH optimization. The test substance is 15 mM H_2O_2 solution.

In Fig. 11a, within the scan rate range of 10–120 mV/s, the CV curves exhibit clear and symmetrical redox peaks. The peak currents increase synchronously with the increase of scan rates, and the peak potential difference slightly increases with the increase of scan rates, preliminarily indicating that the system undergoes a reversible electron transfer process. As can be clearly seen from Fig. 11a, the CV curves at different scan rates all exhibit a pair of symmetrical and distinct redox peaks, indicating that redox reactions are occurring simultaneously on the electrode surface. As the scan rates increase, the currents of the oxidation peaks and reduction peaks increase in tandem, the peak shapes remain symmetrical throughout, and the peak potential difference changes only slightly. This clearly indicates that reversible redox reactions are taking place on the surface of the electrode and that the reaction process is diffusion-controlled [106,107]. Compared with existing literatures, MCHM are versatile [37,43,49]. Furthermore, the raw materials used in MCHM are all low-toxicity substances, making them safer than other chemical materials. In Fig. 11b, both the oxidation peak and reduction peak currents exhibit a highly linear relationship with the square root of the scan rates ($R^2 > 0.99$), further demonstrating the close correlation between the electrode reaction and the diffusion process. According to existing literature reports, researchers have shown that by coating silver-doped ceria composite nanometer powder onto the surface of the electrode, the modified electrode exhibits efficient electrocatalytic oxidation-reduction capability for H_2O_2. Researchers have significantly enhanced the electrochemical sensing performance by coating porous cerium dioxide nanomaterials onto the electrode surface for the detection of H_2O_2 [108,109].

3.6.2 Impedance Test

The impedance experiments are measured in the frequency range of 0.1–100,000 Hz. The detection is carried out using the CV method (Fig. 12a), and then electrochemical impedance spectroscopy is used to detect and read the impedance values for analysis (Fig. 12b). Due to the differences in the material composition of the MCHM, their response performance to the electrochemical sensors shows significant differences. In Fig. 12a, the two oxidation peaks at 0.6 V are clearly visible, and the currents for MCHM is relatively high. According to the relevant literature analysis [110,111], the FTIR spectrum of MCHM shown in Fig. 3a exhibits a broad peak at 3300 cm^{-1} corresponding to the -OH functional group. The presence of -OH

means that -OH activates the -OH group, making it more susceptible to oxidation. Consequently, a distinct oxidation peak appears at around 0.6 V. Through the fitting analysis of the electrochemical EIS spectra, the resistance values of the bare electrode and the MCHM electrode are calculated as 92.59 Ω and 77.12 Ω. The MCHM have the lowest impedance value and a higher electron transfer rate than that of the bare electrode, which in turn confirms that the MCHM have a superior conductivity performance [73,112,113].

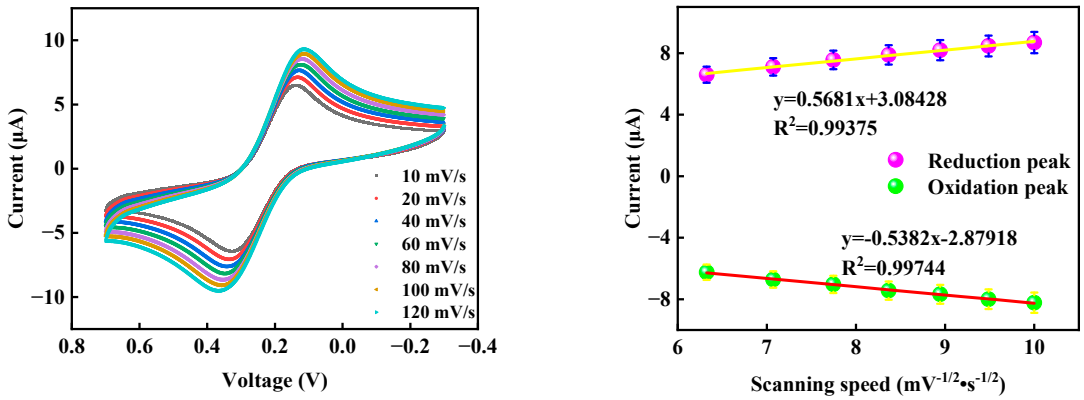

(**a**) (**b**)

Figure 11: (**a**) CV curves at different scan rates; (**b**) Corresponding linear fitting of peak current vs. the square root of scan rates. The test substance is 15 mM H_2O_2 solution.

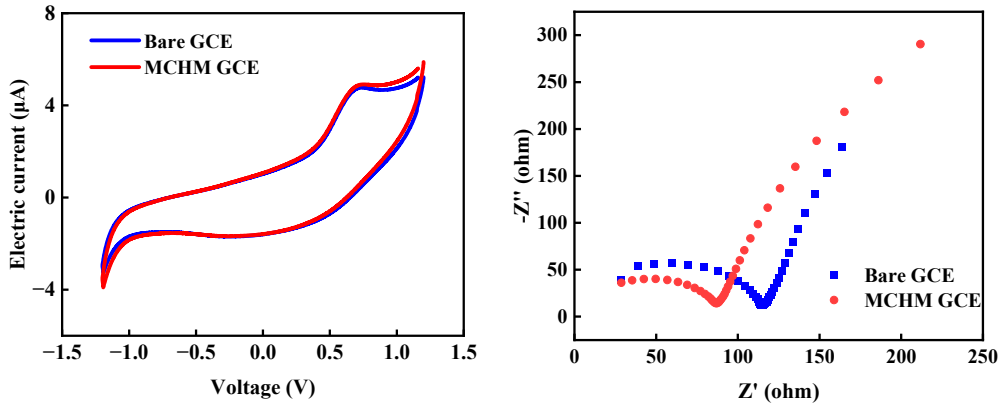

(**a**) (**b**)

Figure 12: (**a**) CV curves; (**b**) EIS spectra. GCE presents a glassy carbon electrode; Z′ presents real impedance; -Z″ presents negative imaginary impedance. The electrolyte used in the impedance experiment is 5 mM $[Fe(CN)_6]^{3-/4-}$ solution.

3.6.3 Research on Selectivity and Anti-Interference of H_2O_2

The selectivity test illustrates that the MCHM are selective for H_2O_2. Better selectivity enables the electrochemical sensor to recognize the target analyte more accurately while more effectively discriminating against interfering components in the test sample (Fig. 13a).

Anti-interference simulates the influence of possible interfering substances in the human physiological environment on the detection results (Fig. 13b). The difference in electrochemical response of this composite-modified electrode to H_2O_2, and a variety of coexisting interfering substances is systematically investigated.

The interfering substances used in this experiment simulate common substances (potassium chloride (KCl), sodium chloride (NaCl)) and biomolecules (glucose (Glu), fructose (Fru), ascorbic acid (AA), uric acid (UA), and dopamine (DA)) in human body fluids, which may coexist with H_2O_2 and affect the accuracy of detection [114].

Fig. 13c shows the lifespan test results of the MCHM sensor for H_2O_2 detection. The response current obtained on the first day is used as the initial reference value to evaluate the storage stability of the sensor. As shown in Fig. 13c, the response of the sensor gradually decreases with increasing storage time. After 3 days, the response current retains 98.21% of its initial value, indicating good short-term stability. The decrease in electrochemical performance may be attributed to the gradual degradation or rearrangement of the sensing interface during storage, partial detachment of the modified materials from the electrode surface, oxidation or aggregation of active components, and reduced accessibility of active sites. These changes may weaken the electron-transfer efficiency and decrease the catalytic/recognizable ability toward H_2O_2, leading to the observed signal decay [115].

The repeatability test reveals that the error of the charge response is small, which provides direct evidence that the MCHM possess excellent reversibility and stability (Fig. 13d). This result further indicates that the electrode surface remains in a relatively stable state throughout the testing process, with no obvious material adsorption, desorption, or other factors that might interfere with the kinetics of the electrochemical reaction. In addition, the small fluctuations in the coulomb response signal confirm the robustness of performance, allowing it to demonstrate outstanding durability and reliability in practical applications. Such properties are of key significance in reducing the experimental error and uncertainty of results in electrochemical detection systems. In summary, these experimental results fully verify the feasibility of the prepared MCHM for H_2O_2 detection in the present study system.

3.6.4 Detection and Analysis Results of H_2O_2

The CV curves of the MCHM (Fig. 14a) show excellent electrochemical performance. The linear fitting result in Fig. 14b shows an LOD of 0.45 μM. The good linearity indicates that the experimental method is reliable and accurate. In addition, the H_2O_2 concentration shows a linear relationship with the coulomb value. This result helps to further elucidate the reaction characteristics [116]. Therefore, it can be shown that the electrochemical properties of the introduced MCHM are stable.

3.6.5 Experimental Results of H_2O_2 Recovery Rates.

In Table 2, it is clearly shown that the recovery rate of farm water is 98.24%, with a RSD of 3.4%. The recovery rate of tap water is 97.183%, with a RSD of 2.59%. The recovery rates of both samples are electrochemical sensing performance toward H_2O_2. LODs of three parallel tests are between 95% and 100%, indicating that this method has good accuracy in complex water quality environments. If the RSD rate is less than 5%, it indicates that the method has good precision and stability.

3.7 Mechanism Analysis of H_2O_2

By modifying the electrode interface with MCHM (Fig. 15), the internal interaction between MCHM and H_2O_2 accelerates electron transfer and promotes ion diffusion, thereby facilitating redox reactions in the electrochemical system. During the detection of H_2O_2 at different concentrations, the detection sensitivity is further improved, background interference is reduced, and signal transmission is enhanced. MCHM possess high hydrophilicity, a three-dimensional porous network structure, and abundant polar functional groups, enabling MCHM to quickly absorb electrolytes and establish continuous ion transmission channels,

thereby significantly reducing ion diffusion resistance. Meanwhile, MCHM are uniformly modified on the electrode surface, effectively reducing the interfacial charge transfer resistance, increasing the effective electrochemical active area [117].

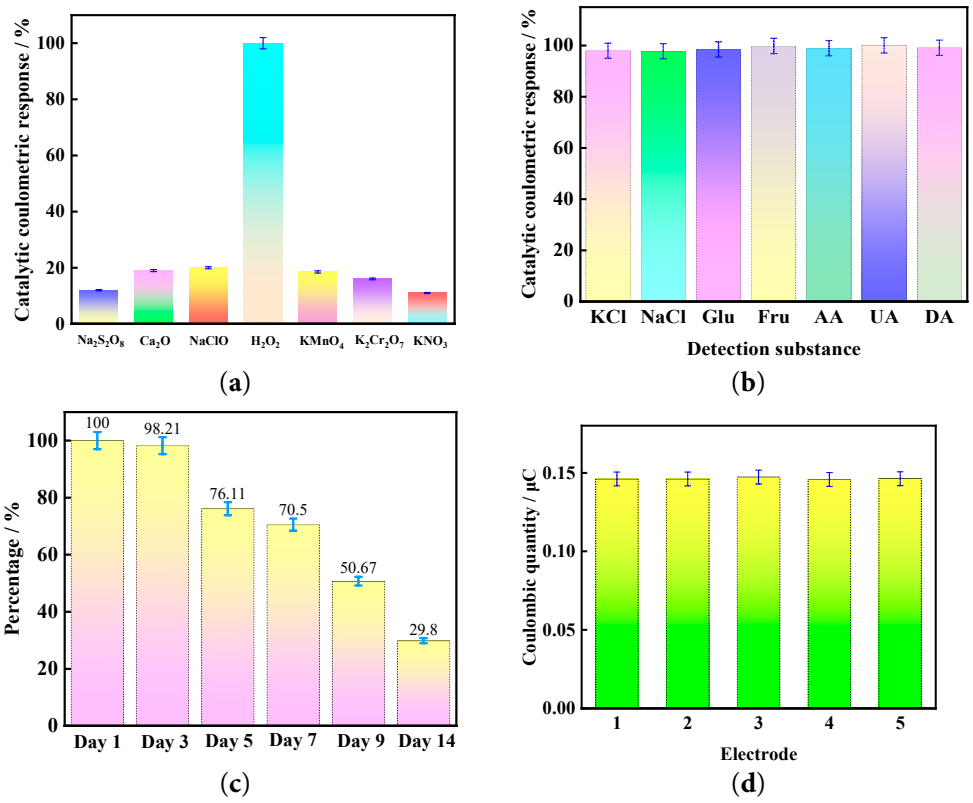

Figure 13: Selectivity, anti-interference, lifespan, and repeatability of the MCHM-modified electrode for H_2O_2 detection. (**a**) Selectivity test against common interfering substances; (**b**) Anti-interference test in the presence of coexisting substances; (**c**) Lifespan; (**d**) Repeatability of MCHM. The electrolyte is always 5 mM PBS solution.

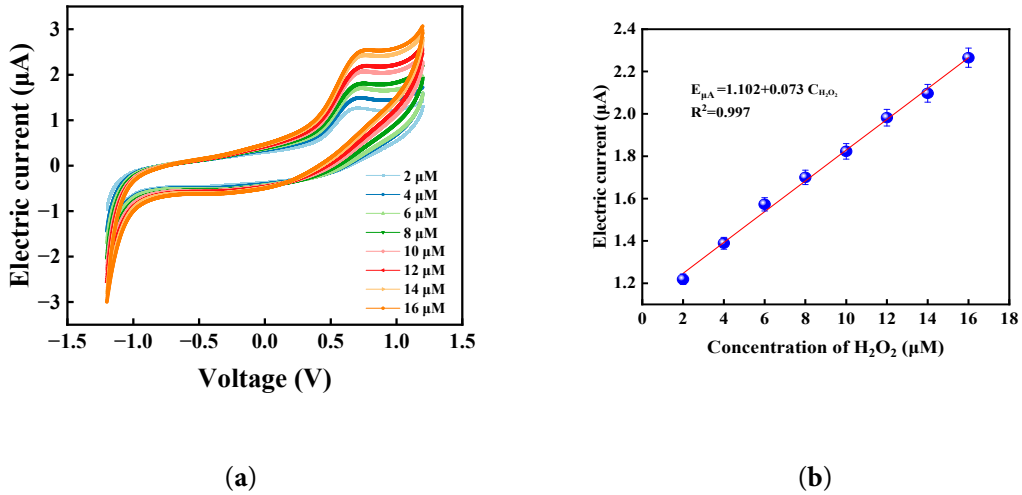

Figure 14: Electrochemical sensing performance of the MCHM-modified electrode for H_2O_2. (**a**) CV curves of the electrode in H_2O_2 solutions with serial concentrations ranging from 2 μM to 16 μM; (**b**) Linear relationship between oxidation peak current and H_2O_2 concentration.

Table 2: Recovery rates of H_2O_2.

Sample	Spiked Concentration (μM)	Total Found (μM)	Recovery Rates (%)	RSDs (%)
Farm water	5	4.995	99.90	3.102
	10	9.786	97.86	3.472
	15	14.544	96.96	3.626
Tap water	5	3.892	97.30	2.371
	10	9.789	98.89	2.456
	15	14.454	96.36	2.956

The CV curves results clearly indicate that MCHM significantly enhance the redox peak while maintaining good reaction reversibility, demonstrating a synergistic promoting effect on electron transfer and ion diffusion. EIS analysis shows a remarkable decrease in charge transfer resistance and improves ion diffusion. This demonstrates that MCHM optimize the electrode interface and enable highly sensitive and stable electrochemical sensing [118].

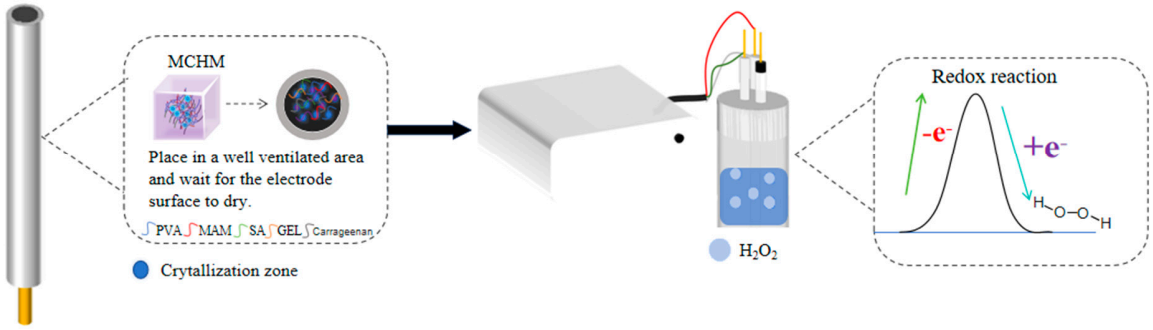

Figure 15: Electrochemical mechanism analysis.

3.8 Comparison with Other Methods

By comparing existing relevant literature data, it is further demonstrated that the MCHM studied in this research exhibit relatively stable performance and demonstrate excellent fluorescent-electrochemical properties in the detection of tartrazine and H_2O_2. As shown in Table 3, the fluorescence detection method for tartrazine provides a low LOD of 0.165 μM together with a wide LR of 0–160 μM, indicating superior analytical performance over several previously reported methods. In addition, the electrochemical detection method for H_2O_2 with a LOD of 0.45 μM and a LR of 2–16 μM, showing satisfactory sensitivity and good potential for practical analysis.

Table 3: Comparison of existing data.

Target Analysis	Sensing Method	LR (μM)	LOD (μM)	Ref.
Tartrazine	Smartphone-based colorimetric	6.2–50	1.8	[119]
	Differential pulse voltammetry	1.57–9.3	0.992	[120]
	Spectrophotometric	0–160	0.165	This work.
H_2O_2	Electrochemical	10–50	0.45	[121]
	Electrochemical	0.2–7.0	12.3	[122]
	Electrochemical	2–16	0.45	This work.

4 Conclusions

The prepared MCHM, with their unique cross-linked framework structure and excellent bifunctional properties, can rapidly respond to tartrazine and H_2O_2, offering the advantages of short testing times, ease of use, and good accuracy. This study comprehensively investigates MCHM's performance in detecting tartrazine and H_2O_2 in water, demonstrating significant potential for application in the field of industrial environmental monitoring and fully realizing MCHM's practical value. MCHM can be further processed into portable rapid test kits, which can be widely used in the food industry for residue screening of synthetic pigments such as tartrazine, compliance testing of food additives such as H_2O_2. MCHM exhibit excellent biocompatibility and film-forming properties, enabling long-term food preservation and reducing reliance on chemical preservatives. Benefiting from the porous network and specific recognition ability, MCHM realize efficient loading and sustained release of bioactive agents, improving their *in vivo* bioavailability and reducing adverse effects. In addition, by introducing flexible conductive substrates and electrochemical signals, optimized MCHM can be developed into wearable smart medical devices, such as sensor patches and flexible detection bracelets. These devices enable real-time monitoring of biochemical indicators in human body fluids, provide early abnormality warnings, and offer new technical support for precise disease diagnosis and health management. At present, limited by the precision and characterization means of the existing testing equipment, this study has not carried out a systematic analysis of the mechanical properties of the prepared composite hydrogels. However, key mechanical properties of the hydrogels, including tensile strength, compressive modulus, and elastic recovery, remain insufficiently studied. Its structural stability under dynamic conditions, such as repeated swelling, deswelling cycles, and long-term immersion, has also not been systematically evaluated, limiting reliable assessment of its practical applicability. In the subsequent research work, the formula and preparation process of hydrogels can be optimized to develop green and non-toxic hydrogel materials derived from natural biomolecules. Precisely construct the hydrogel network structures by adjusting key parameters, including crosslinker dosage, reaction temperature, and time. Meanwhile, the performance testing system is optimized using dynamic mechanical analysis and other professional equipment to systematically characterize its mechanical and related properties. The research focuses on the innovation of bifunctional fluorescent sensing and electrochemical detection, develops new composite hydrogel materials that are environmentally friendly and have low toxicity, and achieves highly selective identification and high-sensitivity detection of more target substances, to provide practical and innovative technological solutions and theoretical support for environmental water quality monitoring and the protection of human health.

Acknowledgement: The authors would like to express their sincere gratitude to the National Natural Science Foundation of China (Project No. U1860112) for its financial support.

Funding Statement: The authors would like to express heartfelt thanks to National Natural Science Foundation of China (project number: U1860112).

Author Contributions: The authors confirm contribution to the paper as follows: study conception and design: Peiqi Zhang, Xiaoliang Hao; data collection: Peiqi Zhang; analysis and interpretation of results: Peiqi Zhang, Xiaoliang Hao, Weifeng Chen; draft manuscript preparation: Peiqi Zhang, Xiaoliang Hao, Weifeng Chen. All authors reviewed and approved the final version of the manuscript.

Availability of Data and Materials: The relevant data can be obtained by contacting the corresponding author via email (haoxiaoliang1980@163.com).

Ethics Approval: Not applicable.

Conflicts of Interest: The authors declare no conflicts of interest.

Abbreviations

The following abbreviations are used in this manuscript:

CQDs	Carbon quantum dots
MAM	Methacrylamide
MCHM	MAM composite hydrogel materials
SA	Sodium alginate
PVA	Polyvinyl alcohol
MPD	M-phenylenediamine
KPS	Potassium persulphate
Bis	N, N'-methylenebisacrylamide
$[Fe(CN)_6]^{3-/4-}$	Potassium hexacyanoferrate(II)
UV-Vis	Ultraviolet-Visible spectroscopy
PTFE	Polytetrafluoroethylene
2D-COS	Two-dimensional correlation spectroscopy
TEM	Transmission electron microscopy
SEM	Scanning electron microscope
FTIR	Fourier transform infrared spectroscopy
XRD	X-ray diffraction
XPS	X-ray photoelectron spectroscopy
PBS	Phosphate buffered saline
CV	Cyclic voltammetry
EIS	Electrochemical impedance spectroscopy
RSD	Relative standard deviation
LOD	Limit of detection
LR	Linear range
GCE	Glassy carbon electrode

References

1. Al-Tohamy R, Ali SS, Li F, Okasha KM, Mahmoud YA, Elsamahy T, et al. A critical review on the treatment of dye-containing wastewater: Ecotoxicological and health concerns of textile dyes and possible remediation approaches for environmental safety. Ecotoxicol Environ Saf. 2022;231:113160. [CrossRef].
2. Khayyat L, Essawy A, Sorour J, Soffar A. Tartrazine induces structural and functional aberrations and genotoxic effects *in vivo*. Toxicol Ind Health. 2017;33(2):147–55.
3. Bhatt D, Vyas K, Singh S, John PJ, Soni I. Tartrazine induced neurobiochemical alterations in rat brain sub-regions. Food Chem Toxicol. 2018;113:322–7. [CrossRef].
4. Essawy AE, Mohamed AI, Ali RG, Ali AM, Abdou HM. Analysis of Melatonin-Modulating Effects Against Tartrazine-Induced Neurotoxicity in Male Rats: Biochemical, Pathological and Immunohistochemical Markers. Neurochem Res. 2023;48(1):131–41. [CrossRef].
5. Fukuzumi S, Lee YM, Nam W. Recent progress in production and usage of hydrogen peroxide. Chin J Catal. 2021;42(8):1241–52. [CrossRef].
6. Torun H, Uluisik S. Postharvest application of hydrogen peroxide affects physicochemical characteristics of tomato fruits during storage. Hortic Environ Biotechnol. 2022;63(3):391–401. [CrossRef].
7. Oloyede A, Ogunleye O, Ajayi O, Adebayo A, Akinyemi A, Omoleye J. Use of hydrogen peroxide vapour for microbiological disinfection in hospital environments: A review. Int J Environ Res Public Health. 2025;22(13):10967804. [CrossRef].
8. Waghmare RB, Annapure US. Effects of hydrogen peroxide, modified atmosphere and their combination on quality of minimally processed cluster beans. J Food Sci Technol. 2017;54(11):3658–65. [CrossRef].

9. Toledo TM, Valerio HP, Melo AT, Gomes RN, Melo TC, Buri MV, et al. Proteomic analysis of hydrogen peroxide-treated human chondrocytes shows endoplasmic reticulum stress, cytoskeleton remodeling, and altered secretome composition. Cell Commun Signal. 2025;23(1):282. [CrossRef].
10. Sies H. Hydrogen peroxide as a central redox signaling molecule in physiological oxidative stress: Oxidative eustress. Redox Biol. 2017;11:613–9. [CrossRef].
11. Xu L, He SS, Li DY, Mei C, Hou XL, Jiang LS, et al. Hydrogen peroxide induces oxidative stress and the mitochondrial pathway of apoptosis in RAT intestinal epithelial cells (IEC-6). Mol Biol. 2016;50(2):270–7. [CrossRef].
12. Shen T, Duan C, Chen B, Li M, Ruan Y, Xu D, et al. Tremella fuciformis polysaccharide suppresses hydrogen peroxide-triggered injury of human skin fibroblasts via upregulation of SIRT1. Mol Med Rep. 2017;16(2):1340–6. [CrossRef].
13. Stein KT, Moon SJ, Sikes HD. Mitochondrial H_2O_2 generation using a tunable chemogenetic tool to perturb redox homeostasis in human cells and induce cell death. ACS Synth Biol. 2018;7(9):2037–44. [CrossRef].
14. di Marzo N, Chisci E, Giovannoni R. The role of hydrogen peroxide in redox-dependent signaling: Homeostatic and pathological responses in mammalian cells. Cells. 2018;7(10):156. [CrossRef].
15. Olenin AY, Olenina EG. Spectrophotometric nonenzymatic determination of hydrogen peroxide using silver nanoparticles. J Anal Chem. 2017;72(2):234–8. [CrossRef].
16. Gill TM, Zheng X. Comparing methods for quantifying electrochemically accumulated H_2O_2. Chem Mater. 2020;32(15):6285–94. [CrossRef].
17. Huang Y, Wang L, Chen B, Zhang Q, Zhu R. Detecting hydrogen peroxide reliably in water via ion chromatography: A method evaluation update and comparison in the presence of interfering components. Environ Sci Water Res Technol. 2020;6(9):2396–404. [CrossRef].
18. Arkin K, Zheng Y, Hao J, Zhang S, Shang Q. Polychromatic carbon dots prepared from *m*-phenylenediamine and urea as multifunctional fluorescent probes. ACS Appl Nano Mater. 2021;4(8):8500–10. [CrossRef].
19. Zhang S, Liu B, Li W, Lin T, Yang H, Pei Y, et al. Highly selective and sensitive fluorescence determination of m-Phenylenediamine. Microchem J. 2021;167:106283. [CrossRef].
20. Xu X, Jerca VV, Hoogenboom R. Bioinspired double network hydrogels: From covalent double network hydrogels via hybrid double network hydrogels to physical double network hydrogels. Mater Horiz. 2021;8(4):1173–88. [CrossRef].
21. Krasnopeeva EL, Panova GG, Yakimansky AV. Agricultural Applications of Superabsorbent Polymer Hydrogels. Int J Mol Sci. 2022;23(23):15134. [CrossRef].
22. Bustamante-Torres M, Romero-Fierro D, Arcentales-Vera B, Palomino K, Magaña H, Bucio E. Hydrogels classification according to the physical or chemical interactions and as stimuli-sensitive materials. Gels. 2021;7(4):182. [CrossRef].
23. Zhang X, Zhang Z, Yang C, Hu Z, Chen Y, Feng L. Cytidine-rich hydrogel as an electrochemical signal amplification strategy for microRNA detection. Analyst. 2022;147(12):2757–63. [CrossRef].
24. Shang X, He SY, Xu Z, Lu W, Zhang W. Hemin-phytic Acid Functionalized Porous Conducting Polymer Hydrogel With Good Biocompatibility for Electrochemical Detection of H_2O_2 Released From Living Cells. Electroanalysis. 2021;33(4):1088–95. [CrossRef].
25. Yu HC, Li CY, Du M, Song Y, Wu ZL, Zheng Q. Improved toughness and stability of κ-carrageenan/polyacrylamide double-network hydrogels by dual cross-linking of the first network. Macromolecules. 2019;52(2):629–38. [CrossRef].
26. Zhao X, Liang J, Shan G, Pan P. High strength of hybrid double-network hydrogels imparted by inter-network ionic bonds. J Mater Chem B. 2019;7(2):324–33. [CrossRef].
27. Wang Z, Kang H, Liu H, Zhang S, Xia C, Wang Z, et al. Dual-network nanocross-linking strategy to improve bulk mechanical and water-resistant adhesion properties of biobased wood adhesives. ACS Sustain Chem Eng. 2020;8(44):16430–40. [CrossRef].
28. Zhang Y, Ren B, Xie S, Cai Y, Wang T, Feng Z, et al. Multiple physical cross-linker strategy to achieve mechanically tough and reversible properties of double-network hydrogels in bulk and on surfaces. ACS Appl Polym Mater. 2019;1(4):701–13. [CrossRef].
29. Dai Y, Wai S, Li P, Shan N, Cao Z, Li Y, et al. Soft hydrogel semiconductors with augmented biointeractive functions. Science. 2024;386(6720):431–9. [CrossRef].

30. Huang H, Xu B, Tan Z, Jiang Q, Fang S, Li L, et al. A facile *in situ* growth of CdS quantum dots on covalent triazine-based frameworks for photocatalytic H_2 production. J Alloys Compd. 2020;833:155057. [CrossRef].
31. Kako K, Kanao E, Ishihama Y, Yamada SK, Kubo T, Tanaka S. Selective fluorescence detection of bovine serum albumin using aggregation-induced emission molecularly imprinted hydrogels. J Mater Chem B. 2025;13(34):7890–8. [CrossRef].
32. Wu Z, Yang X, Wu J. Conductive hydrogel- and organohydrogel-based stretchable sensors. ACS Appl Mater Interfaces. 2021;13(2):2128–44. [CrossRef].
33. Yu X, Li X, Kan L, Pan P, Wang X, Liu W, et al. Double network microcrystalline cellulose hydrogels with high mechanical strength and biocompatibility for cartilage tissue engineering scaffold. Int J Biol Macromol. 2023;238:124113. [CrossRef].
34. Li Z, Lu F, Liu Y. A review of the mechanism, properties, and applications of hydrogels prepared by enzymatic cross-linking. J Agric Food Chem. 2023;71(27):10238–49. [CrossRef].
35. Hou Z, Zhou T, Bai L, Wang W, Chen H, Yang L, et al. Design of cellulose nanocrystal-based self-healing nanocomposite hydrogels and application in motion sensing and sweat detection. ACS Appl Mater Interfaces. 2024;16(28):37087–99. [CrossRef].
36. Dong L, Shan C, Liu Y, Sun H, Yao B, Gong G, et al. Characterization and mechanistic study of heavy metal adsorption by facile synthesized magnetic xanthate-modified chitosan/polyacrylic acid hydrogels. Int J Environ Res Public Health. 2022;19(17):11123. [CrossRef].
37. Wang Y, Yuan K, Shang ZH, Tan GZ, Zhong QJ, He YJ, et al. Construction of nanohydrogels for enhanced delivery of hydrophilic and hydrophobic drugs and improving chemotherapy efficacy. Eur Polym J. 2023;186:111838. [CrossRef].
38. Zou Y, Liu R, Zhong W, Yang W. Mechanically robust double-crosslinked network functionalized graphene/polyaniline stiff hydrogels for superior performance supercapacitors. J Mater Chem A. 2018;6(18):8568–78. [CrossRef].
39. Feng E, Gao W, Li J, Wei J, Yang Q, Li Z, et al. Stretchable, healable, adhesive, and redox-active multifunctional supramolecular hydrogel-based flexible supercapacitor. ACS Sustain Chem Eng. 2020;8(8):3311–20. [CrossRef].
40. Shi Y, Pan L, Liu B, Wang Y, Cui Y, Bao Z, et al. Nanostructured conductive polypyrrole hydrogels as high-performance, flexible supercapacitor electrodes. J Mater Chem A. 2014;2(17):6086–91. [CrossRef].
41. Atef AK, Mostafa TB, El-Sherif HM. Hemocompatible gelatin-glycidyl methacrylate/graphene oxide composite hydrogels for vascular catheter applications. Sci Rep. 2025;15(1):10224. [CrossRef].
42. Xu Y, Yang M, Ma Q, Di X, Wu G. A bio-inspired fluorescent nano-injectable hydrogel as a synergistic drug delivery system. New J Chem. 2021;45(6):3079–87. [CrossRef].
43. Dou Q, Hu D, Gao H, Zhang Y, Yetisen AK, Butt H, et al. High performance boronic acid-containing hydrogel for biocompatible continuous glucose monitoring. RSC Adv. 2017;7(66):41384–90. [CrossRef].
44. Zhai Z, Xu K, Mei L, Wu C, Liu J, Liu Z, et al. Co-assembled supramolecular hydrogels of cell adhesive peptide and alginate for rapid hemostasis and efficacious wound healing. Soft Matter. 2019;15(42):8603–10. [CrossRef].
45. Censi R, Casadidio C, Dubbini A, Cortese M, Scuri S, Grappasonni I, et al. Thermosensitive hybrid hydrogels for the controlled release of bioactive vancomycin in the treatment of orthopaedic implant infections. Eur J Pharm Biopharm. 2019;142:322–33. [CrossRef].
46. Tang Y, Cai X, Xiang Y, Zhao Y, Zhang X, Wu Z. Cross-linked antifouling polysaccharide hydrogel coating as extracellular matrix mimics for wound healing. J Mater Chem B. 2017;5(16):2989–99. [CrossRef].
47. Kamachi Y, Bastakoti BP, Alshehri SM, Miyamoto N, Nakato T, Yamauchi Y. Thermo-responsive hydrogels containing mesoporous silica toward controlled and sustainable releases. Mater Lett. 2016;168:176–9. [CrossRef].
48. Chen XY, Low HR, Loi XY, Merel L, Mohd Cairul Iqbal MA. Fabrication and evaluation of bacterial nanocellulose/poly(acrylic acid)/graphene oxide composite hydrogel: Characterizations and biocompatibility studies for wound dressing. J Biomed Mater Res. 2019;107(6):2140–51. [CrossRef].
49. Kowalski G, Witczak M, Kuterasiński Ł. Structure effects on swelling properties of hydrogels based on sodium alginate and acrylic polymers. Molecules. 2024;29(9):1937. [CrossRef].
50. Kumar V, Sachdev A, Matai I. Self-assembled reduced graphene oxide–cerium oxide nanocomposite@cytochrome *c* hydrogel as a solid electrochemical reactive oxygen species detection platform. New J Chem. 2020;44(26):11248–55. [CrossRef].

51. Tang D, Song H, Yan C, Luo Y, Su X, Ruan S. Hydrogel composite scaffold repairs knee cartilage defects: A systematic review. RSC Adv. 2025;15(13):10337–64. [CrossRef].
52. Wu Z, Zhang P, Zhang H, Li X, He Y, Qin P, et al. Tough porous nanocomposite hydrogel for water treatment. J Hazard Mater. 2022;421:126754. [CrossRef].
53. Aghamirsalim M, Mobaraki M, Jabbarvand M, Sahraian A. Thermosensitive chitosan-hyaluronic acid hydrogel for sustained betamethasone and levofloxacin delivery in corneal wound healing. Transl Vis Sci Technol. 2026;15(3):2. [CrossRef].
54. Lin P, Liu L, He G, Zhang T, Yang M, Cai J, et al. Preparation and properties of carboxymethyl chitosan/oxidized hydroxyethyl cellulose hydrogel. Int J Biol Macromol. 2020;162:1692–8. [CrossRef].
55. Mohammed M, Lai TS, Lin HC. Substrate stiffness and sequence dependent bioactive peptide hydrogels influence the chondrogenic differentiation of human mesenchymal stem cells. J Mater Chem B. 2021;9(6):1676–85. [CrossRef].
56. Liang J, Dong X, Wei C, Kong D, Liu T, Lv F. Phthalocyanine incorporated alginate hydrogel with near infrared fluorescence for non-invasive imaging monitoring *in vivo*. RSC Adv. 2017;7(11):6501–10. [CrossRef].
57. Chen X, Xu W, Jiang Y, Pan G, Zhou D, Zhu J, et al. A novel upconversion luminescence derived photoelectrochemical immunoassay: Ultrasensitive detection to alpha-fetoprotein. Nanoscale. 2017;9(42):16357–64. [CrossRef].
58. Gao XX, Zhou X, Ma YF, Wang CP, Chu FX. A fluorometric and colorimetric dual-mode sensor based on nitrogen and iron Co-doped graphene quantum dots for detection of ferric ions in biological fluids and cellular imaging. New J Chem. 2018;42(18):14751–6. [CrossRef].
59. Liu KQ, Wang ZX, Li F, Li HY, Wang W. Preparation and utilization of carbon dots as a nanoprobe for sensitive detection of tartrazine and palladium (II). Analyst. 2024;149(11):3073–7. [CrossRef].
60. Massah RT, Zambou Jiokeng SL, Liang J, Njanja E, Ma Ntep TM, Spiess A, et al. Sensitive electrochemical sensor based on an aminated MIL-101(Cr) MOF for the detection of tartrazine. ACS Omega. 2022;7(23):19420–7. [CrossRef].
61. Xu D, Lin Q, Chang HT. Recent advances and sensing applications of carbon dots. Small Meth. 2020;4(4):1900387. [CrossRef].
62. Li J, Jiao Y, Feng L, Zhong Y, Zuo G, Xie A, et al. Highly N, P-doped carbon dots: Rational design, photoluminescence and cellular imaging. Microchim Acta. 2017;184(8):2933–40. [CrossRef].
63. Yan T, Zhong W, Yu R, Yi G, Liu Z, Liu L, et al. Nitrogen-doped fluorescent carbon dots used for the imaging and tracing of different cancer cells. RSC Adv. 2019;9(43):24852–7. [CrossRef].
64. Chen Y, Jiao C, Peng X, Liu T, Shi Y, Liang M, et al. Biomimetic anisotropic poly (vinyl alcohol) hydrogels with significantly enhanced mechanical properties by freezing–thawing under drawing. J Mater Chem B. 2019;7(20):3243–9. [CrossRef].
65. Chu W, Ke X, Dong Z, Xie J, Luo J, Li J. Dual crosslinking hydrogels with tunable injectability and stability for bone repair. J Mater Chem B. 2022;10(23):4386–94. [CrossRef].
66. Dong C, Zhou J, Shi D, Song Y, Yu X, Dong W, et al. One-step mild preparation of tough and thermo-reversible poly(vinyl alcohol) hydrogels induced by small molecules. Chem Commun. 2021;57(31):3789–92. [CrossRef].
67. Evans CW, Ho D, Lee PKH, Martin AD, Chin IL, Wei Z, et al. A dendronised polymer architecture breaks the conventional inverse relationship between porosity and mechanical properties of hydrogels. Chem Commun. 2021;57(6):773–6. [CrossRef].
68. Aksu Dönmez Ö, Dinç-Zor Ş, Aşçı B, Şen E. Simultaneous HPLC-DAD determination of pseudoephedrine HCl, sodium benzoate, sunset yellow, and methyl paraben in syrup preparation by use of partial least squares and principal component regression. J Liq Chromatogr Relat Technol. 2019;42(19–20):648–53. [CrossRef].
69. Rejczak T, Tuzimski T. Application of high-performance liquid chromatography with diode array detector for simultaneous determination of 11 synthetic dyes in selected beverages and foodstuffs. Food Anal Meth. 2017;10(11):3572–88. [CrossRef].
70. Miao X, Wang W, Xiong B, Zhou X, Hu J. A separation-free method for simultaneous determination of sucrose and sunset yellow in different abundance by integrating RBI and TL detectors. Anal Methods. 2011;3(3):514. [CrossRef].

71. Myland J. An analytical expression for the current-voltage relationship during reversible cyclic voltammetry. J Electroanal Chem. 1983;153(1–2):43–54. [CrossRef].
72. Matsumoto K, Taniarashi M, Tsutaho Y, Yamada A, Yosho A, Osakai T, et al. Redox reactions between ABTS•$^{+}$ and dihydroxybenzenes as studied by cyclic voltammetry. Anal Sci. 2022;38(1):227–30. [CrossRef].
73. Elgrishi N, Rountree KJ, McCarthy BD, Rountree ES, Eisenhart TT, Dempsey JL. A practical beginner's guide to cyclic voltammetry. J Chem Educ. 2018;95(2):197–206. [CrossRef].
74. Muñoz J, Montes R, Baeza M. Trends in electrochemical impedance spectroscopy involving nanocomposite transducers: Characterization, architecture surface and bio-sensing. Trac Trends Anal Chem. 2017;97:201–15. [CrossRef].
75. Donne SW, Ningsih P. Application of electrochemical impedance spectroscopy to manganese-modified polypyrrole thin films for electrochemical capacitors. ECS Meet Abstr. 2013;MA2013-02(9):677. [CrossRef].
76. Zhao S, Song X, Chai X, Zhao P, He H, Liu Z. Green production of fluorescent carbon quantum dots based on pine wood and its application in the detection of Fe^{3+}. J Clean Prod. 2020;263:121561. [CrossRef].
77. Panwar AS, Singh A, Sehgal S. Material characterization techniques in engineering applications: A review. Mater Today Proc. 2020;28:1932–7. [CrossRef].
78. Olad A, Zebhi H, Salari D, Mirmohseni A, Reyhanitabar A. A promising porous polymer-nanoclay hydrogel nanocomposite as water reservoir material: Synthesis and kinetic study. J Porous Mater. 2018;25(3):665–75. [CrossRef].
79. Sun C, Lux S, Müller E, Meffert M, Gerthsen D. Versatile application of a modern scanning electron microscope for materials characterization. J Mater Sci. 2020;55(28):13824–35. [CrossRef].
80. Jiang C, Lu H, Zhang H, Shen Y, Lu Y. Recent advances on *in situ* SEM mechanical and electrical characterization of low-dimensional nanomaterials. Scanning. 2017;2017:1985149. [CrossRef].
81. Zhao B, Jiang H, Lin Z, Xu S, Xie J, Zhang A. Preparation of acrylamide/acrylic acid cellulose hydrogels for the adsorption of heavy metal ions. Carbohydr Polym. 2019;224:115022. [CrossRef].
82. Bunaciu AA, Aboul-Enein HY, Fleschin S. Recent applications of Fourier transform infrared spectrophotometry in herbal medicine analysis. Appl Spectrosc Rev. 2011;46(4):251–60. [CrossRef].
83. Enders AA, North NM, Fensore CM, Velez-Alvarez J, Allen HC. Functional group identification for FTIR spectra using image-based machine learning models. Anal Chem. 2021;93(28):9711–8. [CrossRef].
84. Arjunan V, Sakiladevi S, Rani T, Mythili CV, Mohan S. FTIR, FT-Raman, FT-NMR, UV-visible and quantum chemical investigations of 2-amino-4-methylbenzothiazole. Spectrochim Acta A Mol Biomol Spectrosc. 2012;88:220–31. [CrossRef].
85. Rahuman MH, Muthu S, Raajaraman B, Raja M. Quantum computational, spectroscopic and molecular docking investigations on 4-Acetylamino-benzoic acid methyl ester: A prospective anticancer drug. Chem Data Collect. 2020;26:100352. [CrossRef].
86. Sugumaran V, Prakash S, Ramu E, Arora AK, Bansal V, Kagdiyal V, et al. Detailed characterization of bio-oil from pyrolysis of non-edible seed-cakes by Fourier Transform Infrared Spectroscopy (FTIR) and gas chromatography mass spectrometry (GC-MS) techniques. J Chromatogr B. 2017;1058:47–56. [CrossRef].
87. Zhao P, Liu X, De La Torre AG, Lu L, Sobolev K. Assessment of the quantitative accuracy of Rietveld/XRD analysis of crystalline and amorphous phases in fly ash. Anal Methods. 2017;9(16):2415–24. [CrossRef].
88. Ghaly M, Masry BA, Abu Elgoud EM. Fabrication of magnesium oxide–calcium alginate hydrogel for scaffolding yttrium and neodymium from aqueous solutions. Sci Rep. 2023;13:15891. [CrossRef].
89. Kondekar NP, Boebinger MG, Woods EV, McDowell MT. *In situ* XPS investigation of transformations at crystallographically oriented MoS_2 interfaces. ACS Appl Mater Interfaces. 2017;9(37):32394–404. [CrossRef].
90. Naohara R, Narita K, Ikeda-Fukazawa T. Change in hydrogen bonding structures of a hydrogel with dehydration. Chem Phys Lett. 2017;670:84–8. [CrossRef].
91. Wang L, Cheng B, Zhang L, Yu J. *In situ* irradiated XPS investigation on S-scheme TiO_2@$ZnIn_2S_4$ photocatalyst for efficient photocatalytic CO_2 reduction. Small. 2021;17(41):2103447. [CrossRef].
92. Yu W, Yu Z, Cui Y, Bao Z. Degradation and speciation of Li salts during XPS analysis for battery research. ACS Energy Lett. 2022;7(10):3270–5. [CrossRef].
93. Solati N, Mobassem S, Kahraman A, Ogasawara H, Kaya S. A comprehensive study on the characteristic spectroscopic features of nitrogen doped graphene. Appl Surf Sci. 2019;495:143518. [CrossRef].

94. Eaton DF. Recommended methods for fluorescence decay analysis. Pure Appl Chem. 1990;62(8):1631–48. [CrossRef].
95. Chang CY, Chang CC, Hsiao TC. Fluorescence intrinsic characterization of excitation-emission matrix using multi-dimensional ensemble empirical mode decomposition. Int J Mol Sci. 2013;14(11):22436–48. [CrossRef].
96. Ojeda CB, Rojas FS. Recent applications in derivative ultraviolet/visible absorption spectrophotometry: 2009–11. Microchem J. 2013;106:1–16. [CrossRef].
97. Tyborski C, Herziger F, Gillen R, Maultzsch J. Beyond double-resonant Raman scattering: Ultraviolet Raman spectroscopy on graphene, graphite, and carbon nanotubes. Phys Rev B. 2015;92(4):041401. [CrossRef].
98. Ohta N. Practical transformations of CIE color-matching functions. Color Res Appl. 1982;7(1):53–6. [CrossRef].
99. Peng HL, Callender R. Mechanism for fluorescence quenching of tryptophan by oxamate and pyruvate: Conjugation and solvation-induced photoinduced electron transfer. J Phys Chem B. 2018;122(25):6483–90. [CrossRef].
100. Lasch P, Noda I. Two-dimensional correlation spectroscopy (2D-COS) for analysis of spatially resolved vibrational spectra. Appl Spectrosc. 2019;73(4):359–79. [CrossRef].
101. Ryu IS, Liu X, Jin Y, Sun J, Lee YJ. Stoichiometric analysis of competing intermolecular hydrogen bonds using infrared spectroscopy. RSC Adv. 2018;8(42):23481–8. [CrossRef].
102. Hniopek J, Schmitt M, Popp J, Bocklitz T. PC 2D-COS: A principal component base approach to two-dimensional correlation spectroscopy. Appl Spectrosc. 2020;74(4):460–72. [CrossRef].
103. Salahinejad M, Sadjadi S, Abdouss M. Investigating fluorescence quenching of cysteine-functionalized carbon quantum dots by heavy metal ions: Experimental and QSPR studies. J Mol Liq. 2021;334:116067. [CrossRef].
104. Chang DH, Ou CL, Hsu HY, Huang GJ, Kao CY, Liu YH, et al. Cooperativity and site-selectivity of intramolecular hydrogen bonds on the fluorescence quenching of modified GFP chromophores. J Org Chem. 2015;80(24):12431–43. [CrossRef].
105. Chakik FE, Kaddami M, Mikou M. Optimization of physico-chemical parameters of hydrogen production by electrolysis of water. In: Proceedings of the 2018 Renewable Energies, Power Systems & Green Inclusive Economy (REPS-GIE); 2018 Apr 23–24; Casablanca, Morocco. p. 1–6. [CrossRef].
106. Islam MN, Abir AY, Ahmed J, Faisal M, Algethami JS, Harraz FA, et al. Electrocatalytic oxygen reduction reaction at FeS_2-CNT/GCE surface in alkaline medium. J Electroanal Chem. 2023;941:117568. [CrossRef].
107. Hao C, Wang L, Wen F, Xiang J, Li L, Hu W, et al. Layer structured bismuth selenides Bi_2Se_3 and Bi_3Se_4 for high energy and flexible all-solid-state micro-supercapacitors. Nanotechnology. 2018;29(8):085401. [CrossRef].
108. Ali MY, Abdulrahman HB, Howlader MM. Hydrogen peroxide electrochemical sensor using green synthesized silver nanoparticles. Surf Interfaces. 2025;74:107662. [CrossRef].
109. Yu Z, Lv S, Ren R, Cai G, Tang D. Photoelectrochemical sensing of hydrogen peroxide at zero working potential using a fluorine-doped tin oxide electrode modified with BiVO4 microrods. Microchim Acta. 2017;184(3):799–806. [CrossRef].
110. Jin YF, Chai YY, Liu Y, Guo J, Yan H. Experimental study on the evolutionary characteristics of silicified coal functional groups during oxidation/pyrolysis. Combust Sci Technol. 2023;195(11):2491–509. [CrossRef].
111. Islam MR, Beg MDH. Dispersion characteristics of hydroxyl and carboxyl-functionalized multi-walled carbon nanotubes in polyester nanocomposites. J Polym Eng. 2018;38(8):759–65. [CrossRef].
112. Xu N, Riley J, Kilner JA. Nonlinear electrochemistry impedance spectroscopy and its applications. ECS Meet Abstr. 2012;MA2012-02(16):1933. [CrossRef].
113. Xiao H, Tao Z, Bai H, Wang H, Fu Y, Si N, et al. State of charge effects on the parameters of electrochemical impedance spectroscopy equivalent circuit model for lithium ion batteries. IOP Conf Ser Earth Environ Sci. 2020;474(5):052038. [CrossRef].
114. Yang M, Yang X, Wang M, Jiang R. A sensitive and selective electrochemiluminescent sensor for dopamine based on the inhibition of dual-stabilizer-capped CdS quantum dot electrochemiluminescence. Anal Methods. 2017;9(15):2334–41. [CrossRef].
115. Mouais T, Kittaneh OA, Abdulmajid M. The effects of electrode physical parameters on the statistical life models of Li-ion battery. In: Proceedings of the 2021 IEEE International IOT, Electronics and Mechatronics Conference (IEMTRONICS); 2021 Apr 21–24; Toronto, ON, Canada. p. 1–5. [CrossRef].
116. Fu R, Lu Y, Ding Y, Li L, Ren Z, Si X, et al. A novel non-enzymatic glucose electrochemical sensor based on CNF@Ni-Co layered double hydroxide modified glassy carbon electrode. Microchem J. 2019;150:104106. [CrossRef].

117. Sandford C, Edwards MA, Klunder KJ, Hickey DP, Li M, Barman K, et al. A synthetic chemist's guide to electroanalytical tools for studying reaction mechanisms. Chem Sci. 2019;10(26):6404–22. [CrossRef].

118. Marcus RA. On the theory of electrochemical and chemical electron transfer processes. Can J Chem. 1959;37(1):155–63. [CrossRef].

119. Jacinto C, Maza Mejía I, Khan S, López R, Sotomayor MDPT, Picasso G. Using a smartphone-based colorimetric device with molecularly imprinted polymer for the quantification of tartrazine in soda drinks. Biosensors. 2023;13(6):639. [CrossRef].

120. Mehmandoust M, Erk N, Karaman O, Karimi F, Bijad M, Karaman C. Three-dimensional porous reduced graphene oxide decorated with carbon quantum dots and platinum nanoparticles for highly selective determination of azo dye compound tartrazine. Food Chem Toxicol. 2021;158:112698. [CrossRef].

121. Althomali RH, Alamry KA, Hussein MA, Guedes RM. Hybrid PANI@dialdehyde carboxymethyl cellulose/ZnO nanocomposite modified glassy carbon electrode as a highly sensitive electrochemical sensor. Diam Relat Mater. 2022;122:108803. [CrossRef].

122. Sönmez Çelebi M, Kırlak Kara S. Non-enzymatic hydrogen peroxide sensor based on palladium-decorated poly(thionine) modified glassy carbon electrode. J Chin Chemical Soc. 2024;71(5):482–92. [CrossRef].